

Seeing beyond the spikes: reconstructing the complete spatiotemporal membrane potential distribution from paired intra- and extracellular recordings

Domokos Meszéna^{1,2} , Anna Barlay^{3,4} , Péter Boldog^{3,4} , Kristóf Furuglyás^{3,5}, Dorottya Cserpán³ , Lucia Wittner^{1,2,6} , István Ulbert^{1,2,6}  and Zoltán Somogyvári^{3,7} 

¹Institute of Cognitive Neuroscience and Psychology, Research Centre for Natural Sciences, Budapest, Hungary

²Faculty of Information Technology and Bionics, Pázmány Péter Catholic University, Budapest, Hungary

³Theoretical Neuroscience and Complex Systems Research Group, Department of Computational Sciences, Wigner Research Center for Physics, Budapest, Hungary

⁴Bolyai Institute, University of Szeged, Szeged, Hungary

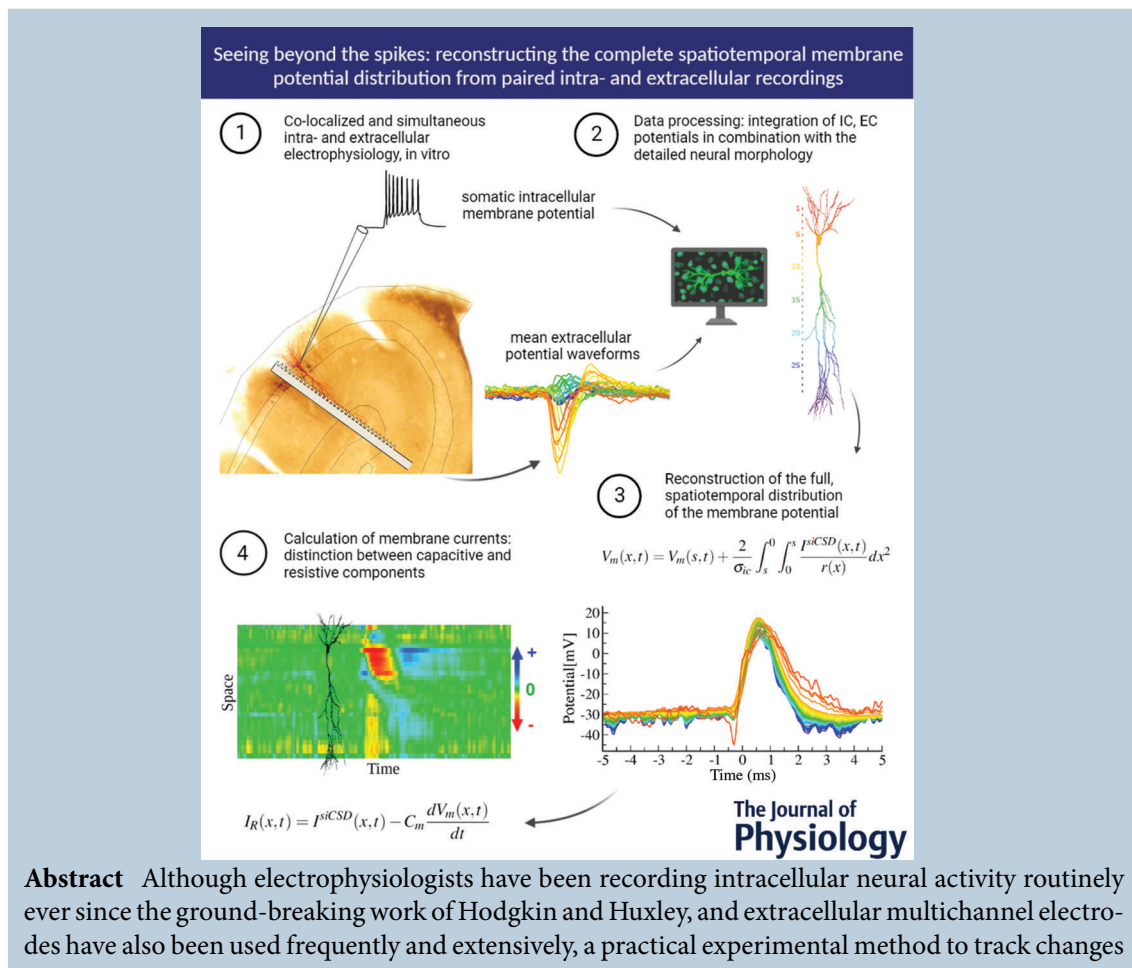
⁵Doctoral School of Physics, Faculty of Science, ELTE Eötvös Loránd University, Budapest, Hungary

⁶National Institute of Clinical Neurosciences, Budapest, Hungary

⁷Axoncord LLC, Budapest, Hungary

Handling Editors: Katalin Toth & Richard Naud

The peer review history is available in the Supporting information section of this article (<https://doi.org/10.1113/JP283550#support-information-section>).



in membrane potential along a complete single neuron is still lacking. Instead of obtaining multiple intracellular measurements on the same neuron, we propose an alternative method by combining single-channel somatic patch-clamp and multichannel extracellular potential recordings. In this work, we show that it is possible to reconstruct the complete spatiotemporal distribution of the membrane potential of a single neuron with the spatial resolution of an extracellular probe during action potential generation. Moreover, the reconstruction of the membrane potential allows us to distinguish between the two major but previously hidden components of the current source density (CSD) distribution: the resistive and the capacitive currents. This distinction provides a clue to the clear interpretation of the CSD analysis, because the resistive component corresponds to transmembrane ionic currents (all the synaptic, voltage-sensitive and passive currents), whereas capacitive currents are considered to be the main contributors of counter-currents. We validate our model-based reconstruction approach on simulations and demonstrate its application to experimental data obtained *in vitro* via paired extracellular and intracellular recordings from a single pyramidal cell of the rat hippocampus. In perspective, the estimation of the spatial distribution of resistive membrane currents makes it possible to distinguish between active and passive sinks and sources of the CSD map and the localization of the synaptic input currents, which make the neuron fire.

(Received 30 June 2022; accepted after revision 28 November 2022; first published online 13 December 2022)

Corresponding authors D. Meszéna: Institute of Cognitive Neuroscience and Psychology, Research Centre for Natural Sciences, Budapest, H-1117, Hungary. Email: meszenadomi@gmail.com; Z. Somogyvári: Wigner Research Centre for Physics, Department of Computational Sciences, Theoretical Neuroscience and Complex Systems Research Group, Budapest, H-1121, Hungary. Email: somogyvari.zoltan@wigner.mta.hu

Abstract figure legend In this work, we show that it is possible to reconstruct the complete spatiotemporal distribution of the membrane potential of a single neuron, with the spatial resolution of an extracellular probe, by combining single-channel somatic patch-clamp and multichannel extracellular potential recordings during action potential generation. The model-based membrane potential reconstruction uses the detailed morphology of the neuron and allows us to distinguish between the two major but previously hidden components of the current source density (CSD) distribution: the resistive and the capacitive currents. This distinction provides a clue to the clear interpretation of the CSD analysis, because the resistive component corresponds to transmembrane ionic currents (all the synaptic, voltage-sensitive and passive currents), whereas capacitive currents are considered to be the main contributors of counter-currents. In perspective, estimation of the spatial distribution of resistive membrane currents makes it possible to localize the synaptic input currents, which make the neuron fire.

Key points

- A new computational method is introduced to calculate the unbiased current source density distribution on a single neuron with known morphology.
- The relationship between extracellular and intracellular electric potential is determined via mathematical formalism, and a new reconstruction method is applied to reveal the full spatiotemporal distribution of the membrane potential and the resistive and capacitive current components.
- The new reconstruction method was validated on simulations.
- Simultaneous and colocalized whole-cell patch-clamp and multichannel silicon probe recordings were performed from the same pyramidal neuron in the rat hippocampal CA1 region, *in vitro*.
- The method was applied in experimental measurements and returned precise and distinctive characteristics of various intracellular phenomena, such as action potential generation, signal back-propagation and the initial dendritic depolarization preceding the somatic action potential.

Introduction

The key variable of neuronal activity is the membrane potential (V_m); it influences the voltage-sensitive channels providing the non-linear temporal dynamics of neurons, serving as the basis of action potential generation. In the quest for a mathematical description of membrane potential dynamics, a key element in Hodgkin and Huxley's (1952) famous experiments was the so-called 'space-clamp' method, in which a thin axial platinum wire was inserted along the giant axon of the squid, which made the whole length of the axon isopotential, eliminating the spatial dependence of the membrane potential. Therefore, the dynamical system formed by the non-linear voltage-dependent channels was simplified to a system that could be described by ordinary differential equations. This made model fitting and reconstruction possible using contemporary computation. This simplification led to the successful description of the biophysical mechanism underlying action potential generation, but it left the spatial distribution and dynamics of the membrane potential largely unexplored.

The spatial distribution of the membrane potential not only describes the different dynamics of different parts of the neurons, but axial currents are also driven by the spatial gradient of the membrane potential. Therefore, the spreading of postsynaptic potentials can be controlled by and synaptic input signals can be integrated by the spatial distribution of the membrane potential, as described in the cable theory applied by Rall (1962) and many others, extending the work of Hodgkin and Huxley.

The discretization of the cable models has led to the constantly growing family of conductance-based multicompartmental models. These models, consisting of hundreds or thousands of compartments, provide an unprecedented precision and detailed description of the electrophysiological process during synaptic integration and action potential generation. Multicompartmental models are usually fitted to electrophysiological recordings obtained by single somatic patch-clamp data. However, single patch-clamp recordings at the somatic region will never allow us to observe other distinct, local neuronal events, such as the very specific behaviour of the axon initial segment or the active Ca^{2+} and Na^+ spikes generated by more distal dendrites that are believed to

be essential for dendritic integration, computation and synaptic plasticity (Buccino et al., 2022; Gidon et al., 2020; Kumar et al., 2022). Building a well-grounded compartmental model requires a detailed description of channel dynamics, in addition to their density and distribution along the whole neuron, which is still a major challenge. Besides the difficulty of equipping the models with the right amount of different channels, an important missing component for understanding the whole input-output dynamic of the neurons is the spatiotemporal distribution of the synaptic input. Larkum et al. (1999) applied a heroic effort to obtain multiple simultaneous intracellular signals from a single cortical layer 5b pyramidal cell via three patch-clamp micropipettes, one placed in the soma and two in the main apical dendrite. Hay et al. (2011) used these triple recordings to fit their multicompartmental model and were able to reproduce complex, active dendritic behaviours. However, it is very challenging to perform the somatic patch-clamping itself properly (even with one pipette), and attempting the same with two additional dendritic pipettes simultaneously on the same neuron is nearly impossible. It is clear that other modalities and supplementary measurements are necessary to provide the missing fine-scale, the subcellular properties of the measured single neuron. Despite the rapid parallel development of advanced optical recording techniques using fluorescent indicators, such as two-photon Ca^{2+} imaging, or voltage imaging via genetically encoded voltage indicators, still no experimental technique has managed to provide measurements of the whole-cell distribution of the membrane potential with temporal resolution comparable to the time scale of synaptic currents and action potential generation and spatial resolution comparable to axonal paths arriving onto a single neuron across multiple cortical layers.

The intracellular (IC) electrochemical activity of neurons inevitably generates extracellular (EC) changes owing to the transmembrane currents, thus EC potential patterns around a neuron also carry information about the changes in the membrane potential. The EC potential elicited by transmembrane currents varies dynamically in time and space, because numerous currents can be superimposed at a given location in the EC medium (Buzsáki, 2004; Buzsáki et al., 2012). Thus, the EC potential contains

Domokos Meszéna is a postdoctoral research associate at the Integrative Neuroscience Group (headed by István Ulbert) at the Research Centre for Natural Sciences in Budapest, Hungary. Domokos obtained his PhD degree from Pázmány Peter Catholic University, Faculty of Information Technology and Bionics, with a specialization in experimental neuroscience and neurotechnology. His present research focuses on combining various electrophysiological tools and advanced imaging techniques of cellular and systems neuroscience. The recorded multimodal signals are then used to establish a realistic experimental ground-truth dataset for supporting various model-based calculations, including the cellular-level current source density analysis.



all the summed signals of multiple synaptic inputs and spiking outputs, in addition to different local and further (volume-conducted) activities in the region where the EC recording electrode is located (Einevoll et al., 2013; Pettersen et al., 2012; Somogyvari et al., 2012). Although the basic biophysical principles of EC potential generation have been known for a long time, the relationship between the IC and EC potential patterns is still poorly understood. It is noteworthy that extracellular single-unit activities are typically three orders of magnitude smaller (in the range of tens to hundreds of microvolts) than the magnitude of an intracellular action potential. Thus, spatial inhomogeneity of the EC potential is typically neglected in the models describing IC membrane potential changes. Nevertheless, they are non-negligible from the EC point of view when we aim to describe the emergence of the EC potential patterns and the relationship between EC and IC potentials.

Here, we outline our new roadmap to bridge the gap between EC and IC potentials, with the experimental and theoretical steps to be solved, along with the previous attempts and solutions from the literature.

- (1) In order to connect EC and IC potential patterns properly in an ideal experimental environment, one has to perform simultaneous and colocalized extracellular and intracellular recordings. These experiments must be both 'colocalized' and 'simultaneous' because only spatiotemporally synchronized recordings can provide accurate information about the interconnection between EC and IC potential patterns. According to current literature, the inter-probe distance, the corresponding soma–electrode distance when obtaining whole-cell recordings, should be in the range of tens of micrometres, but maximally $<100\ \mu\text{m}$ to achieve signals with high-quality EC voltage traces; although the limit for the maximal range is still controversial (Buzsáki et al., 2012; Einevoll et al., 2013; Henze et al., 2000; Scott et al., 2012; Somogyvari et al., 2012).
- (2) The simultaneously recorded EC potential certainly contains the signal from the nearby neuron recorded intracellularly but might also contain much more. The signs of the activity of the whole local neural network are mixed in the extracellularly recorded electrical signals. Thus, one has to ensure that the EC potential pattern in the analysis originates exclusively from the IC-recorded neuron. Although there is no perfect technique to filter out the contribution of only one neuron, the spike-triggered average (STA), an averaged waveform based on the timing of the IC spike, ensures that only those EC potentials contribute to the mean that are highly correlated with the IC activity of the recorded neuron. In a similar manner to the macroscopic event-related potentials, various events could be used to generate meaningful event-related potentials on the micro-scale, such as *in vitro* stimulations of a specific pathway or sensory inputs measured *in vivo*.
- (3) The third step connects the EC potential to the net membrane current by applying the current source density (CSD) calculation. The difficulty of this step stems from the non-unique inverse solution of the Poisson equation, describing the extracellular spread of the electrical potential. A unique solution would require numerous *a priori* assumptions about the source. This is done by different CSD methods under different assumptions about the geometry of the sources. At the population level, the traditional one-dimensional (1D) CSD assumes homogeneous (infinite) laminar sources (Nicholson & Freeman, 1975), and the inverse CSD (iCSD) method uses laminar cylindrical sources with a finite and predefined diameter (Pettersen et al., 2006). The kernel CSD (kCSD) method approximates the source with three-dimensional (3D) Gaussian blobs. At the single-neuron level, spike CSD (sCSD) describes the source as a line source parallel to the electrode and estimates the cell–electrode distance using an auto-focus algorithm based on the measured signal (Somogyvari et al., 2012). If the morphology of the cell is known, it can be included in the inverse solution to make the CSD calculation more precise. The single-cell kernel CSD (skCSD) method (Cserpán et al., 2017) calculates the CSD distribution on the known morphology of a neuron by using 1D Gaussian kernel functions to approximate the smooth CSD distributions along the dendritic and axonal processes. This method provides a very good estimation of the CSD distribution in a cell if all the neural processes lie at approximately the same distance from the electrode system. However, if there are significant differences between the distances of different neural processes, the method projects much higher CSD amplitudes to the closer processes than to the distant ones. To avoid this problem, in this work we introduce a new CSD calculation method, called the single-cell inverse CSD (siCSD) method, to calculate the CSD on a neuron with known morphology.
- (4) The last and most challenging step is to connect the CSD to the IC membrane potential. Furthermore, knowing the spatiotemporal distribution of the membrane potential would allow the distinction between resistive and capacitive membrane components, which is necessary to interpret the observed CSD distributions correctly. To the best of our knowledge, there have been only a few attempts in the literature to cross this obstacle, trying to reconstruct the membrane potential distributions at a population level, but none of them has attempted

membrane potential reconstruction at the level of single neurons (Chizhov et al., 2009, 2015). Gratiy et al. (2011) calculated the CSD and the subsequent EC potential caused by localized synaptic inputs by using multicompartmental models. However, several obstacles appeared in avoiding the calculation of the inverse solution; after the inverse transformation, all of the calculated synaptic profiles had zero mean, even if the original synaptic input did not. This means that the forward transformation, the mapping from the synaptic input to the CSD, projected the problem into a zero-mean subspace, preventing the correct inversion of the synaptic profiles. The zero-space problem defined by Gratiy et al. (2011) implies that the EC potential pattern does not contain enough information by itself to reconstruct the IC membrane potential based only on EC measurements.

Here, we present a new approach, showing that the missing information can be supplied by an additional single-channel intracellular measurement, thus simultaneous multichannel EC and single-channel IC potential recordings make the reconstruction of the full spatiotemporal distribution of the IC membrane potential possible. Using this method, the IC membrane potential can be determined with the spatial resolution of the EC recordings along the whole neuron. Moreover, we also show that the reconstruction of membrane potential makes it possible to distinguish between the two components of the net membrane current, and therefore the CSD can be divided into the densities of resistive and capacitive currents. This distinction provides a clue to the clearer interpretation of the CSD distribution, because the resistive component contains all the active channel currents including both synaptic and voltage-sensitive currents, and only a small amount of passive resistive counter-current, whereas the capacitive current corresponds to the majority of passive counter-currents. Thus, estimation of the spatial distribution of the resistive membrane current allows us to distinguish between active and passive sinks and sources of the CSD map and to localize the synaptic input currents, which make the neuron fire. In the following sections, we present the experimental realization of paired IC and EC measurements, together with the reconstruction of cell morphology, serving as ground-truth data for further model-based calculations.

Methods

Parallel EC and IC measurements *in vitro*

Our protocols followed the guidelines of the Hungarian Act of Animal Care and Experimentation (1998; XXVIII, section 243/1998). The Animal Care and Experimentation

Committee of the Hungarian Academy of Sciences and the Animal Health and Food Control Station approved the experimental design (licence no. PEI/001/2290-11/2015). Efforts were made to minimize the suffering of the animals. For the purpose of this paper, we have used only one representative multi-modal dataset collected from a single animal (male, young adult Wistar rat, 280 g). We followed our experimental procedures developed for earlier *in vitro* recordings described elsewhere (Cserpán et al., 2017; Meszéna et al., 2019). Before the experiment, the animal was deeply anaesthetized with isoflurane (minimum of 0.2 ml per 100 g body weight), quickly decapitated, and its brain carefully removed and dipped into cold (2–3°C), oxygenated (95% O₂ and 5% CO₂) cutting solution. The cutting solution had the following composition (mM): 250 sucrose, 26 NaHCO₃, 10 D-glucose, 1 KCl, 1 CaCl₂ and 10 MgCl₂. Approximately 500-μm-thick horizontal slices containing the whole hippocampal formation were cut with a vibratome (VT1200s; Leica, Nussloch, Germany) from both hemispheres. Slices were incubated in a standard artificial cerebrospinal fluid solution at room temperature (20–22°C) for ≥1 h before use. The recording was performed at a physiological temperature (37°C) with a standard recording artificial cerebrospinal fluid containing (mM): 124 NaCl, 26 NaHCO₃, 10 D-glucose, 4 KCl, 2 CaCl₂ and 2 MgCl₂. In the recording chamber, a custom-made dual-perfusion system was used by circulating both the top and the bottom surfaces of the slices with relatively high perfusion speed (>10 ml min⁻¹) to provide better oxygenation, similar to *in vivo* conditions. In these conditions, population events (e.g. sharp wave ripples) and single-unit activities could be detected reliably (Hajos et al., 2009; Ting et al., 2014).

The whole-cell current-clamp recording was performed at 20 kHz sampling frequency from a CA1 pyramidal cell located in the closest vicinity to the extracellular contact sites. The micropipette electrode was made from a borosilicate glass capillary (GC120F-10; Harvard Apparatus, Edenbridge, UK) and pulled by a Flaming/Brown micropipette puller (model P-1000; Sutter Instruments, Novato, CA, USA). The micropipette had an initial resistance of 8 MΩ. The intracellular recording was performed using an internal pipette solution of the following composition (mM): 125 potassium gluconate, 20 KCl, 10 Hepes, 10 Di-Tris-salt phosphocreatine, 0.3 Na-GTP, 4 Mg-ATP, 10 NaCl and 0.008 biocytin (pH adjusted to 7.3, 290–300 mosmol l⁻¹). We also added the following fluorescent dyes to the intracellular solution (for 100 μl): 0.5 μl of 5 mM Alexa 594 (25 μM) and 1 μl of 10 mM fluo-4 (100 μM). The IC signal was recorded using a MultiClamp 700B amplifier (Axon Instruments, Union City, CA, USA) and digitized with the Digidata 1550A (Molecular Devices, Sunnyvale, CA, USA). Data

acquisition was visualized with pClamp10 software (Molecular Devices).

In the following sections, we provide a brief description of every step of the experimental data collection and of the tissue processing. The IC and EC recording devices, in addition to their corresponding locations and orientation on the slice, are shown in Fig. 1. Please note the successfully achieved parallel positioning between the EC probe and the main apical axis of the patch-clamped cell (in Fig. 1D and E). Colocalized multichannel extracellular potentials were recorded using a custom-designed, single-shank, high-density silicon probe carrying 32 protruding laminar contact sites. This minimally invasive probe was developed and optimized in our laboratory to improve brain slice recordings, because its spiky contact sites can slightly penetrate the tissue below the surface dead-cell layer of the resected brain slice (Meszéna et al., 2019). The contact site layout has an inter-contact distance of 25 μm . Figure 1A depicts the complete microelectrode with its curved microelectromechanical system (MEMS) design, bonding, wire carrying printed circuit board and the Omnetics connector. Figure 1B is a scanning electron microscopic photograph of the probe end that shows the protruding laminar, spiky contact sites, and Fig. 1C shows the implantation angle and positioning of the silicon probe under the two-photon microscope objective. Recording of the extracellular local

field potential (LFP) and spiking activity was performed in the closest vicinity of the patched CA1 pyramidal cell. Our *in vitro* electrophysiology set-up was built under a two-photon laser scanning microscopy system (Femtonics, Budapest, Hungary). The detailed steps in the experimental protocol were as follows.

When the freshly cut horizontal hippocampal slice was transferred into the recording chamber and the CA1 pyramidal layer was found and checked to be optimally oriented for insertion, the multichannel extracellular electrode was inserted parallel to the main apical dendritic axis of the CA1 pyramidal cells. Protruding contact sites were penetrated to a depth of $\sim 25 \mu\text{m}$ beneath the slice surface. Naturally, it is very challenging to find completely parallel cellular processes in the close vicinity of the EC probe. Even if the x - y plane is almost perfectly aligned (as in our case), there is an inevitable angle in the z -direction between the cellular axis and the laminar probe, meaning that the somatodendritic axis pointing towards the inside of the slice will gradually move away from the electrode contact sites that remain in the same z -plane. We allowed 15 min for the brain tissue around the inserted EC probe to settle before attempting colocalized patch-clamp recording. Somatic whole-cell patch clamping was performed in current-clamp mode to monitor the sub-threshold membrane potential fluctuations, in addition to the above-threshold spontaneous firing of the neuron,

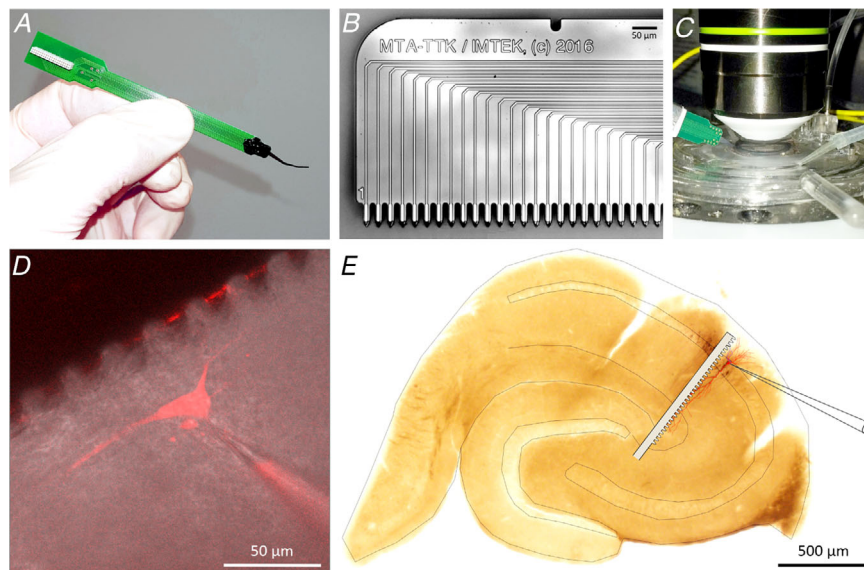


Figure 1. The experimental set-up and device locations

A, the custom-made 32-channel angled *in vitro* silicon probe. B, scanning electron microscopic photograph of the linear, protruding contact site layout. C, positioning of the silicon probe under the two-photon microscopy objective before the insertion. D, close-up of the simultaneous and colocalized recording arrangement. A single CA1 pyramidal cell (in red) is passively filled and visualized by the fluorescent Alexa 594 dye via somatic whole-cell patch clamp. The glass micropipette is visible on the lower right, and the penetrating spiky contact sites of the EC probe appear as a large black silhouette on the top left. E, Neurolucida reconstruction of the detailed neural morphology (in red) after *post hoc* histological processing of the slice. Schematic positions of the two recording devices are shown around the reconstructed CA1 pyramidal cell.

by applying a small and continuous holding current with a constant value of +80 pA. In simultaneous IC–EC mode, a 3-min-long session was recorded, the duration of which was sufficiently short to maintain the physiological conditions of the neuron located very close to the penetrated EC probe, but also long enough to collect a reasonable number of spikes for analysis. For signal acquisition, we used the INTAN RHD2000 FPGA-based system (InTan Technologies, Los Angeles, CA, USA). The acquisition system was connected to an external laptop via a USB 2.0 connection. Wide-band signals (0.1 Hz to 7.5 kHz) were recorded with 16-bit resolution, at a sampling rate of 20 kHz. Data containing 3-min-long (continuous-mode) recordings were saved to internal network storage for further analysis.

As a final step in the experimental session, a volumetric two-photon *z*-stack projection was performed by the microscope to reveal the approximated 3D neuronal morphology and cell–electrode distances immediately. The field of view of the *z*-stack projection was set to cover both the EC probe location and main cellular compartments (soma, apical trunk region and proximal apical and basal dendrites). Figure 1D shows a single-depth photograph of the *z*-stack projection including the soma and proximal dendrites of the patched neuron, in addition to the silhouettes of the IC–EC recording devices.

After the completed experiment, the EC probe was slowly withdrawn and cleaned by immersing it into 1% Tergazyme solution (Sigma-Aldrich, St Louis, MO, USA) for ≥ 30 min, followed by rinsing it with distilled water. Also, the brain slice was carefully removed from the recording chamber and stored overnight in 4% paraformaldehyde with 15% picric acid in 0.1 M phosphate buffer (PB, pH 7.4) at 4°C.

On the day after the experiment, the fixed slice was resectioned (Leica 1200S, Wetzlar, Germany) at 60 μ m and freeze-thawed above liquid N₂ in 0.1 M PB containing 30% sucrose. We followed a histological analysis similar to the one published by Kerekes et al. (2014). In this protocol, endogenous peroxidase activity was blocked by 1% H₂O₂ in Tris-buffered saline for 10 min. Cells containing neurobiotin tracer molecules were revealed with the avidin–biotinylated horseradish complex reaction (Vector; 1.5 h, 1:250) using 3,3'-diaminobenzidine-tetrahydrochloride (Sigma; 0.05 M in Tris buffer, pH 7.6) as the chromogen. At the end, sections were osmicated (20 min, 0.5% OsO₄), dehydrated in ethanol and mounted in Durcupan (ACM; Fluka, Buchs, Switzerland). When all histological steps (fixation, reslicing and the precipitation of neurobiotin) had been successfully completed and the neuronal processes of the filled cell became visible and traceable, neuronal morphology was reconstructed digitally in 3D by the Neurolucida system (MBF Bioscience, Williston,

VT, USA). Figure 1E shows the complete dendritic arborization (in red) of the neuron, its overlaid position in the hippocampal slice, and the schematic visualizations of the IC–EC recording devices.

Data processing

The recorded intracellular and extracellular signals were processed, analysed and visualized using custom-written Scilab, Python and MATLAB scripts (MATLAB2018b; The MathWorks, Natick, MA, USA).

The coordinates of the electrode contact sites were determined in two steps. First, the tips of the electrode traces in the tissue were marked in the Neurolucida reconstruction. Second, a line was fitted to the tip coordinates and the contact site locations were interpolated, resulting in evenly distributed contact point locations with 25 μ m inter-electrode distances. Very low frequencies were filtered out from the EC potential by a low-cut Gaussian Fourier filter with a 1 Hz cutting frequency. Four channels having low signal quality were identified: three channels (channels 1, 31 and 32) were omitted from the ends of the electrode system, and one channel (29) was interpolated from the neighbouring channels by a third-order spline each time instance.

Spike-triggered averages are considered extracellular footprints of individual neurons recorded on the closely located EC contact sites. As a first step, IC potential recordings were smoothed by a 0.25-ms-long moving window average, and the time instances of the spike occurrences were determined by a 0 mV upward threshold crossing of the smoothed IC potential. Applying this event detection algorithm, 763 spikes were detected on the 180-s-long recording file. For epoching, 100-ms-long symmetrical time windows were cut around the time points of IC spikes on all EC channels. In order to avoid distortion of prespike and postspike subthreshold events in the STAs, 13 spikes with interspike intervals <50 ms were deleted, because otherwise they would have contaminated other individual epochs. Finally, epochs were averaged for the remaining 750 spike times on all EC channels and for the raw, unsmoothed IC channel.

Calculation of the transfer matrix elements and the spatial integration were implemented in discrete steps using the coordinates of the Neurolucida compartments. The morphological description consists of 2544 compartments for our measured CA1 pyramidal neuron and 4260 compartments for the Hay model. The surface of each compartment was defined as the surface area of a truncated cone. The temporal derivative of the membrane potential was approximated by the difference of the consecutive time steps. Units for computational parameters were as follows: length in micrometres, time

in seconds, voltage in microvolts, surface in micrometres squared, T matrix in ohms micrometres squared, the inverse of the T matrix in siemens per micrometre squared, siCSD in picoamperes per micrometre squared, the whole membrane current and the capacitive and resistive current components in picoamperes, and axial conductivity in siemens per micrometre. The sCSD values estimated per unit length were in siemens per micrometre, the values in the T matrix in ohms micrometres, and T inverse in siemens per micrometre in the sCSD method. The following fix parameters were applied by the siCSD method: the specific extracellular conductivity ($\sigma_{EC} = 3 \times 10^{-7} \text{ S } \mu\text{m}^{-1}$), specific intracellular conductivity ($\sigma_{IC} = 6 \times 10^{-6} \text{ S } \mu\text{m}^{-1}$) and specific membrane capacity ($C_m = 0.9 \times 10^{-14} \text{ F } \mu\text{m}^{-2}$).

Simulations

In order to understand the relationship between extra- and intracellular potentials and to test the reconstruction procedure, multicompartmental neural simulations were conducted using different software packages. Simulation of a passive ball-and-stick neuron (Fig. 2) was implemented in Scilab. In this simulation, the dendritic diameter was $5 \mu\text{m}$, the somatic diameter $10 \mu\text{m}$, the dendritic compartment length $25 \mu\text{m}$, the membrane resistance $10^3 \Omega \text{ cm}^2$ and the axial specific resistance $200 \Omega \text{ cm}$. The discretized cable equation was solved in 18 compartments by a simple forward Newton method with $0.05 \mu\text{s}$ time steps. The extracellular potential (V^{EC}) was calculated in $50 \mu\text{m}$ distance, parallel to the neuron. The ball-and-stick neuron with passive dendrites

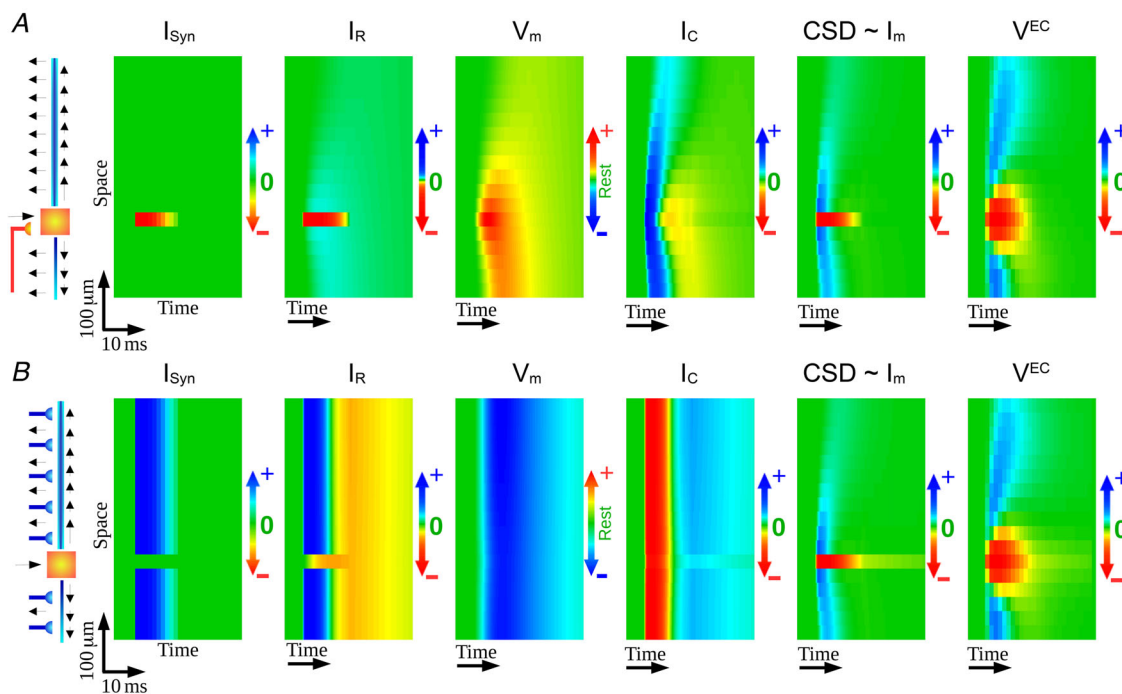


Figure 2. The relationship between intracellular and extracellular variables

Simulated experiments showing the relationship of intracellular and extracellular variables as spatiotemporal colour-coded maps, in response to synaptic current pulses

Warm colours correspond to mostly excitatory events: inward currents, which are considered to be negative by the extracellular literature, depolarization (positive deviation from the resting state) of the membrane potential (V_m) and negative deflection of the extracellular potential (V^{EC}). Conversely, cold colours indicate the inhibitory events, while green indicates zero current, zero V^{EC} and the resting V_m . The length of the time arrows is 10 ms. *A*, a spatially confined pulse of excitatory synaptic current (I_{syn}) initiates the event. The resistive current distribution (I_R) is dominated by a depolarizing, inward, negative current peak (red) accompanied by much smaller outward counter-currents around and after (pale blue). The resulting positive (red) membrane potential change spreads along the cell in a slightly asymmetric manner, while decaying over time and space. The capacitive current (I_C) component corresponds to the local charge accumulation during changes in V_m . The spreading pattern in I_C marks the propagating depolarization in V_m . The corresponding net membrane current (I_m) is proportional to the current source density (CSD) and equals the sum of I_R and I_C . The I_m forms a spreading source–sink–source triplet in space. Note that the sum of I_m on the whole cell is zero in each time instance, whereas this is true for neither I_R nor I_C . The complex triphasic V^{EC} is measured by a multichannel probe, placed parallel at a distance of $50 \mu\text{m}$ from the neuron. *B*, same graphs as in *A*; however, the event is initiated by an extended inhibitory synaptic pulse all along the dendrites but not on the soma. This impulse causes a completely different V_m pattern, a massive hyperpolarization throughout the whole cell, but the identical CSD pattern and thus the same measurable V^{EC} .

but an active soma was implemented in the software package NEURON (Carnevale & Hines, 2006), and V^{EC} was calculated over a distance of 50 μm by using LFPy (Lindén et al. 2014). The length of the neuron was 500 μm , consisting of fifty 10- μm -long dendritic compartments. The dendritic diameter was 4 μm , and the diameter of the soma was 20 μm . The membrane resistance was set to $3 \times 10^4 \Omega \text{ cm}^2$, the intracellular resistivity was 123 $\Omega \text{ cm}$, and the membrane capacitance was 1 $\mu\text{F cm}^{-2}$. Standard Hodgkin–Huxley-type Na^+ and K^+ channels were set in the soma to produce action potentials. Membrane potential, net current, capacitive current and resistive current components were saved from the simulation as ground truth and compared with the reconstructed values.

In order to test the reconstruction procedure on a neuron model with complex morphology and complex dynamics, the model of Hay et al. (2011) was simulated in NEURON. The model had 4260 compartments. Membrane potential, net CSD, capacitive current density and resistive current density, as a sum of passive, h-type, sodium, potassium and calcium currents were saved from the simulation. The net CSD was calculated as the sum of capacitive and resistive currents. These data were used as ground truth and compared with the reconstructed values. The EC potential was calculated by a custom Scilab script from the net transmembrane current at 50 μm resolution. The virtual electrode was roughly parallel to the neuron, and the distance from the soma was 115 μm . In the model, axial resistance was defined as 100 $\Omega \text{ cm}$, the specific capacitance was 1 $\mu\text{F cm}^{-2}$ at the soma and 2 $\mu\text{F cm}^{-2}$ at the dendrites to account for the dendritic spines. Thus, these values were also used in the reconstruction.

Results

Relationship between intracellular and extracellular variables: simulations

Figure 2 shows that even a single, spatially and temporally confined synaptic current pulse evokes complex spatiotemporal patterns of currents and potentials in a passive neural model, both intra- and extracellularly. Before we analyse the relationship between the dynamics of intra- and extracellular variables more deeply, a number of notes should be given on different sign conventions. In the majority of the intracellular literature, starting from the Hodgkin–Huxley equations, the inward current is considered to be positive. In this convention, the positive synaptic current causes positive membrane potential change, hence depolarization. On the contrary, in the extracellular literature, the inward flow of positive ions is considered to be negative, corresponding to a sink in the CSD. Assuming that the extracellular surface of the membrane is positive, because this is generally the case,

the inward positive direction corresponds to the passive sign convention, used more in electrical engineering, whereas the inward negative direction corresponds to the active sign convention more generally used in physics.

Here, we intend to connect the intracellular and the extracellular phenomena, but we try to remain consistent with both traditions. Therefore, our calculation will involve a change of viewpoint. The V^{EC} and all types of currents (I^{CSD} , I_{R} , I_{C} and I_{Syn}) will be written according to the extracellular (active) sign convention, whereas the membrane potential (V_{m}) will be described according to the intracellular (passive) sign convention. Thus, the inward membrane current is considered to be negative, corresponding to the EC sinks, but this causes positive change, a depolarization in the membrane potential. However, in order to express the physiological activating effect and to be consistent with the extracellular literature, negative currents and negative EC potential, and also the positive deviations from the IC resting membrane potential, will be represented by warm colours on the maps throughout this paper.

In the first simulation, events were initiated by a localized inward synaptic current at the soma, corresponding to a cation inflow that depolarizes the cell. This is considered to be negative according to the extracellular convention but marked by hot colours owing to its excitatory effect on the neuron (Fig. 2A).

The time course of the synaptic current was described by an alpha function, as follows:

$$I_{\text{Syn}}(t) = \frac{t}{\alpha} e^{-t/\alpha} \quad (1)$$

The simulation lasted for 30 ms, the spatial extension of the cell was 400 μm , the synaptic stimulation lasted for 10 ms, and $\alpha = 1.5 \text{ ms}$ was used.

Considering the IC membrane potential (V_{m}), the effect of a point-like stimulus or a synaptic input spreads away as a slightly asymmetrically widening Gaussian blob, according to the diffusion process described by the cable equation. This spreading depolarization causes a proportional outflow of ions through the passive (leakage) membrane conductance. Without active currents, the synaptic (red) and the leak currents (pale blue) together give the full resistive (transmembrane) current (I_{R}). It should be noted that the sum of the resistive currents along the whole cell was non-zero; the sum of positive counter-currents was only 10% of the sum of the absolute value all currents, and the maximal amplitude of positive counter-current was only 1.5% of the synaptic amplitude in this case.

The capacitive current, I_{C} , has the opposite sign to I_{Syn} during the first phase of the stimulation, while the V_{m} is rising, and I_{C} changes its sign when V_{m} starts to decay. This is the phase when the equalization of the spatial distribution of the charges takes place. The neighbouring

capacitors formed by the closest membrane segments start to recharge the segment that was discharged by the synaptic event, while they lose their charge; the depolarization is dispersed. The recharging appears as a prolonged current sink close to the synaptic site, extending well beyond the end of the synaptic stimulation while involving farther and farther current sources.

Meanwhile, the net membrane current flow (CSD) is monotonous in time; its sign does not change. The CSD on the cell forms a spreading triphasic spatial distribution, which equals the sum of I_R and I_C . Note, that the sum of these 1D CSD maps is zero for each time instance, in contrast to the resistive membrane current, I_R , or the capacitive membrane current, I_C . The measurable EC potential corresponds to the blurred version of the CSD distribution.

In the second simulation (Fig. 2B), a completely different spatial distribution of synaptic current was applied to the same cell model. A homogeneous inhibitory synaptic input was applied all along both dendrites of the neuron but not at the soma. The time course of the stimulation was the same as in the previous case.

This large inhibitory current caused massive and nearly homogeneous hyperpolarization along the whole cell, spreading to the soma as well. Despite the very different intracellular phenomena on V_m , I_R and I_C , the spatiotemporal CSD pattern elicited by this stimulation is surprisingly similar to the previous one, caused by a localized excitation. Moreover, the resulting extracellular potential is practically indistinguishable from the previous one.

These two simulated examples clearly show that the IC membrane potential cannot be determined based solely on the extracellular potential. The key point of our solution is the fusion of extracellular and intracellular information; while the extracellular measurement carries information about the spatial variability of the membrane potential, the (temporary variable) baseline of the V_m is missing from it. Thus, the solution of the inverse problem should fuse the one-channel IC V_m measurement to the information available in the spatially extended V^{EC} measurement to achieve the full reconstruction of the membrane potential and the resistive current.

The CSD calculation

Assuming a homogeneous and isotropic volume conductor around the neuron, the EC potential and the current source density (I^{CSD}) are connected by the Poisson equation:

$$I^{CSD}(r, t) = -\sigma_{EC} \nabla^2 V^{EC}(r, t) \\ = -\sigma_{EC} \left(\frac{\partial^2 V^{EC}(r, t)}{\partial x^2} + \frac{\partial^2 V^{EC}(r, t)}{\partial y^2} + \frac{\partial^2 V^{EC}(r, t)}{\partial z^2} \right) \quad (2)$$

where σ_{EC} is the specific conductance of the extracellular medium and r is the 3D position of the measurement. In our calculations, $\sigma_{EC} = 3 \times 10^{-7} \text{ S } \mu\text{m}^{-1}$ was used (Varona et al., 2000).

Equation (2) inherently assumes that the EC potential, $V^{EC}(r, t)$, is known at every point in space. Naturally, we can only approximate this with some clever simplifying assumptions and the corresponding appropriate measurement set-ups. In the following subsections, we summarize the former attempts, their advantages and their drawbacks.

Estimation of I^{CSD} without known cell morphology

Regarding the first step of the inverse solution, the CSD calculation on single neurons, two different tasks can occur, depending on whether the morphology of the neuron is known. If the morphology is not known, then the best choice for calculating CSD distribution on a single neuron is the sCSD method (Somogyvari et al., 2012). In contrast, if the neuron is successfully filled and reconstructed after the recording, then there are two choices: skCSD (Cserpán et al., 2017) is applicable if one can ensure that all the neural processes are at about the same distance from the electrode system, or the newly presented siCSD method, which does not rely on this assumption, could also be applied.

Owning only 1D EC potential measurements and neglecting the potential gradients in the perpendicular directions, the traditional 1D CSD (I^{1D}) can be used to calculate the CSD distribution in a simplified form, as follows:

$$I^{1D}(x, t) = -\sigma_{EC} \frac{\partial^2 V^{EC}(x, t)}{\partial x^2} \quad (3)$$

However, this method implicitly assumes large planar sources, which do not fit to the properties of single-neuron sources.

The assumptions of the sCSD method (Somogyvari et al., 2012) fit better to the single-neuron current sources. This method approximates the single neuron with a discretized line source parallel to the electrode, estimates its distance from the electrode, and calculates the sCSD as an inverse solution:

$$I^{sCSD} = T^{-1}(d) V^{EC} \quad (4)$$

where T^{-1} is the inverse of the T Poisson matrix, and d is the estimated distance between the cell and the electrode. The elements of T are given as:

$$T_{ij}(d) = \frac{1}{4\pi\sigma_{EC}\sqrt{(x_i - x_j)^2 + d^2}} \quad (5)$$

where x_i and x_j are the positions of the i^{th} source element and the j^{th} electrode, respectively.

Furthermore, the sCSD method estimates the cell–electrode distance by maximizing a spikiness measure $S(d)$ with respect to d distance:

$$S(d) = \max \left(\frac{-I_i}{|I|} \right) - \text{mean} \left(\frac{-I_i}{|I|} \right) \quad (6)$$

where $|I|$ is the Euclidean norm of the CSD vector, I .

This original form of the sCSD method has been extended here by a Lagrange multiplier imposing the zero-sum constraint to the net membrane current on the whole cell. For this reason, the T matrix has been extended by an additional row, containing constant $\lambda = 1000$ values, the Lagrange multipliers, while the V^{EC} vector has been extended by a zero element for each time moment. These additions implement the constraint equation:

$$\lambda \sum_i I_i = 0 \quad (7)$$

This extension makes the inverse problem over-determined, thus it does not result in exactly zero current sum: the higher the λ , the more the equation is forced towards zero.

The sCSD method is a good approximation if the morphology of the cell is unknown and estimates the unknown cell–electrode distance as well. However, if the real morphology of the neuron is available, this information could be incorporated into the CSD calculation by a proper method and could make it more accurate. The first such method was the skCSD method (Cserpán et al., 2017), which described the smooth CSD distribution along with the known morphology of the neuron by using Gaussian kernel functions. The skCSD method results in precise CSD estimations on the neuron, if all the processes of the neuron are nearly equidistant to the electrode array; for example, a horizontal cell in the retina laid onto an electrode grid. In contrast, if different parts of the neuron are at very different distances relative to the electrode array, the skCSD method will be strongly biased towards the nearest parts.

Our new method to approximate current source density on a single neuron: the siCSD method

To be able to reconstruct the intracellular membrane potential, V_m , from the extracellular V^{EC} of a neuron with known morphology, we need a new CSD calculation method that uses the known morphology of the neuron but is free from the bias of the skCSD method. Here, we introduce a new, single-cell inverse CSD calculation method called siCSD, directly designed for 1D electrode systems, which can meet these requirements.

The current source density on the neuron has been calculated from the EC STA potential pattern by our new siCSD method in each time instance. The whole morphology of the cell has been reconstructed by NeuroLucida, and the resulting morphological description has been transferred to Python in ASCII format.

As a first step of the siCSD calculation, the morphology was divided into slices perpendicular to the 1D electrode array. Each compartment of the cell was clustered into the slice according to the closest electrode. The slices are delineated by the middle points between the electrodes, hence they have equal thicknesses, and there are two slices at the two ends that are open and cover all the excess neural processes.

Next, the CSD was assumed to be equal on all neural compartments belonging to the same slice. This corresponds to the laminar organization of synaptic layers of the hippocampus and, in general, of the cortex. Furthermore, similar laminar source assumptions are used by the traditional 1D CSD method and by the line source model used in the sCSD method (Somogyvari et al., 2005, 2012) and the cylindrical laminar source assumption of the columnar inverse method (Pettersen et al., 2006). However, in our case, the laminar source is restricted to the real morphology of the neuron. The linearities of the electric fields and of the potentials allow for the summation of the effect of every compartment within a slice, resulting in a single weight factor that expresses the potential generated by a whole slice on an electrode. The weight factors between every slice and every electrode form a square transfer matrix, T . Considering the infinite volume conductor approximation, the elements of T are given as:

$$T_{ij} = \frac{1}{4\pi\sigma_{\text{EC}}} \sum_{k=1}^{N_i} \frac{A_{ik}}{d_{ik,j}} \quad (8)$$

The investigated neuron was $\sim 75 \mu\text{m}$ deep in the tissue, and the tips of the electrodes were at $h = 25 \mu\text{m}$ depth below the surface of the tissue. The surface of the slice was covered by artificial cerebrospinal fluid, and the higher conductance of this solution (close to the saline) modified the field of the neuron. The modified potential around the neuron was calculated by the mirror image method, following Ness et al. (2015). However, instead of an infinite series of mirror image charges, only the first mirror image correction term was considered, because the contributions of the further terms were negligible owing to the large ($500 \mu\text{m}$) thickness of the slice.

The corrected T_{ij} elements of the transfer matrix are given as:

$$T_{ij} = \frac{1}{4\pi\sigma_{\text{EC}}} \sum_{k=1}^{N_i} A_{ik} \left(\frac{1}{d_{ik,j}} + \frac{W_{\text{TS}}}{d'_{ik,j}} \right) \quad (9)$$

Where N_i is the number of compartments within the slice i , A_{ik} is the surface of the k^{th} compartment within the slice i , $d_{ik,j} = \sqrt{(x_{ik} - x_j)^2 + (y_{ik} - y_j)^2 + (z_{ik} - z_j)^2}$ is the distance between the k^{th} compartment of the i^{th} slice and the j^{th} electrode, $d'_{ik,j} = \sqrt{(x_{ik} - x_j)^2 + (y_{ik} - y_j)^2 + (z_{ik} - z_j + 2h)^2}$ is the distance of the mirror image from the electrode if h was the depth of the electrode system under the surface of the tissue. The W_{TS} factor of modification depends on the conductance of the EC tissue (σ_{EC}) and the saline (σ_{Sal}):

$$W_{TS} = \frac{\sigma_{EC} - \sigma_{Sal}}{\sigma_{EC} + \sigma_{Sal}} \quad (10)$$

where σ_{Sal} was estimated to be 1.5×10^{-6} based on Ness et al. (2015).

The generated T transfer matrix (Fig. 3A) is generally invertible but ill posed, thus Tikhonov regularization (Tikhonov & Arsenin, 1977) was used to stabilize the inverse. The resulting inverse matrix (T^+) was then used to calculate the CSD distribution on the slices:

$$I^{\text{siCSD}} = T^+ \times V^{\text{EC}} = (T^T T + \alpha^2 I)^{-1} T^T V^{\text{EC}} \quad (11)$$

where T^T is the transpose of the T matrix, and $\alpha^2 I$, a diagonal regularization matrix, was used where I is the identity matrix and α is the regularizing factor (Fig. 3B).

The optimal regularization factor depends on the V^{EC} data (Fig. 3G). Thus, it was determined by minimizing the 'leave-one-out' cross-validation error on the spike-triggered V^{EC} data, similar to the optimal kernel width determination in the study by Cserpán et al. (2017). The possible α^2 values were scanned logarithmically from 10^{-10} to 10^{20} . For each α^2 value, the I^{siCSD} distribution was calculated on the neuron by using the V^{EC} of all but one electrode (eqn 11). Based on the determined I^{siCSD} distribution, the EC potential was reconstructed at the position of the missed electrode by using the T matrix (eqn 9) and compared to the real measured V^{EC} value at that site. The root mean squared error (RMSE) was calculated by sequentially omitting each electrode and comparing the measured and the reconstructed V^{EC} values for the whole 10-ms-long time window around the spike. The RMSE as a function of $\log(\alpha^2)$ is shown in Fig. 3C. The search was refined around the minimum, and the optimal $\alpha^2_{\text{opt}} = 2 \times 10^{11}$ was determined. The leave-one-out reconstructions of the V^{EC} patterns, where all potential values were replaced by their reconstructed V^{EC} values, are shown in Fig. 3D–F, for the moment of highest V^{EC} amplitude. Values of α^2 too low resulted in noisy V^{EC} reconstruction (Fig. 3E), whereas values of α^2 too high over-smoothed the V^{EC} pattern (Fig. 3F). The best-fitting reconstruction belongs to the optimal regularization factor α^2_{opt} (Fig. 3D).

Both sCSD and skCSD methods calculate CSD per unit length (in picoamperes per micrometre) along the dendrites, whereas the traditional CSD is expressed as volume CSD units of picoamperes per micrometre cubed. However, in the new siCSD method we assume constant CSD per unit membrane surface within every slice, thus siCSD is measured in units of picoamperes per micrometre squared. Along with this, the new siCSD method incorporates the known diameters of the compartments into the CSD calculations, because the A_{ik} surface of a cylindrical compartment of length l_{ik} is $A_{ik} = 2\pi r_{ik} l_{ik}$, and the surface of the soma was approximated by a sphere $A_s = 4\pi r_s^2$ of radius $r_s = 10 \mu\text{m}$.

Finally, the results of the new siCSD and the traditional tCSD analysis of the STA EC potential have been compared. Both the STA EC potential pattern (Fig. 3G) and the spatiotemporal CSD patterns (Fig. 3H–J) are represented as heatmaps, where the end of the colour scales corresponds to the absolute amplitude maxima on all graphs.

It is clear that even the V^{EC} map shows the initiation site and the propagation of the action potential as a negative (red) wave. The action potential was initiated at the fifth channel and propagated into both the basal and the apical directions. This main negative wave was completed by a positive (blue) wave along the apical dendrites and followed by another positive inflection after the spike at the somatic region. It should be noted that the main negative component of the V^{EC} around the soma is accompanied by a small (yellow) secondary one around the distal apical region.

The siCSD map (Fig. 3H) clearly shows the initiation of the action potential, which generates a short and distinct sink on the basafourth to fifth channels, followed by the largest and more prolonged sink on the soma, located at the sixth channel. The action potential back-propagation is traceable up to 10 channels on the apical dendrite. Compared with the V^{EC} map, the small but continuous influxes before the action potential initiation at the distal apical dendrites and in the basal region are new features. The positive wave accompanying the back-propagation became more pronounced, and basal counter-currents appeared beside the main somatic sink and source.

The result of the traditional tCSD method (Fig. 3I) shows that the signal-to-noise ratio of the V^{EC} pattern is not satisfactory for this type of analysis. The noise contaminating the V^{EC} pattern overrides any meaningful pattern in the tCSD map. Although the *post hoc* smoothing of the tCSD by a five-channel-long spatial Gaussian kernel eliminated the majority of the spatial noise and made the back-propagation pattern visible again, it blurred the somatic sources and sinks and resulted in strange boundary effects at the basal end of the electrode system (Fig. 3J).

Membrane potential and resistive membrane current reconstruction on single neurons

The key point in our membrane potential reconstruction method is that the CSD in itself, owing to its zero-sum constraint, does not carry enough information for membrane potential reconstruction. However, if the CSD distribution is known, the missing information that

remains is only one degree of freedom at each moment of time. Thus, the parallel intracellular recording is included in the solution, which provides the missing information and anchors the inverse solution to the physiological constraints.

To connect the extracellular and the intracellular membrane potential and the components of the

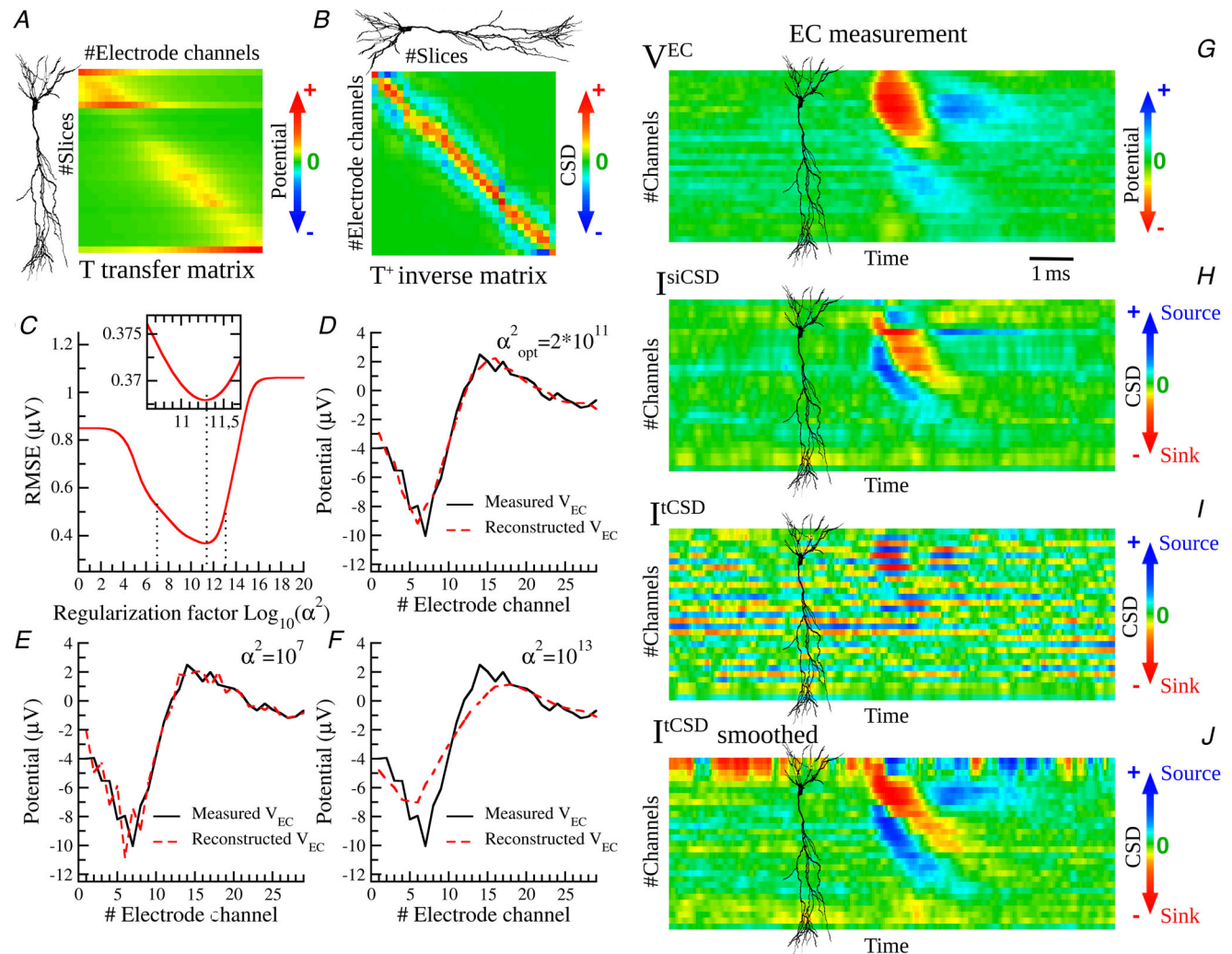


Figure 3. The single-cell inverse current source density (siCSD) method

The single-cell inverse current source density method and its comparison with the traditional current source density method on a real, measured extracellular potential pattern during action potential generation

A, the colour-coded transfer matrix (T) connects the slices of the neuron (rows) to the electrodes (columns). Calculation of T includes the real morphology of the neuron and the coordinates of the electrodes. Rows of T correspond to the extracellular potential (V^{EC}) pattern generated by each slice with unit current source density (CSD) activity per membrane area. B, regularized inverse T^+ of T allows the calculation of CSD distribution, based on the V^{EC} patterns. C, search for the optimal regularization parameter (α^2): root mean squared error (RMSE) of the leave-one-out reconstruction procedure. Inset, zoom to the minimum of RMSE. D, leave-one-out reconstruction (dashed red line) of V^{EC} (continuous black line) at the moment of the highest amplitude with the optimal regularization. E, regularization too small results in noisy leave-one-out reconstruction. F, regularization too large results in over-smoothed reconstruction. G, the spike-triggered average of $n = 750$ V^{EC} patterns used in the analysis. The colour-coded spatiotemporal map shows the ± 5 ms window around the spike. H, the single-cell inverse current source density (siCSD) distribution during the spike with the optimal regularization. I, the noisy result of the traditional current source density (tCSD) analysis. J, the tCSD distribution is smoothed spatially by a Gaussian filter.

membrane current, the derivation of the cable equation should be described first.

The membrane current can be expressed as current per unit length i_m or per unit surface I_m where $i_m = 2\pi r I_m$ and r is the radius of the neural process. The total membrane current i_m is the sum of the capacitive i_C and the resistive i_R membrane currents, also measured in unit lengths:

$$i_m(x, t) = i_C(x, t) + i_R(x, t) \quad (12)$$

The resistive current comprises the passive currents, the currents through the ligand-dependent synaptic conductances, and the voltage-dependent channels, whereas the capacitive current describes the charge accumulation on the membrane:

$$i_C(x, t) = 2\pi r(x) C_m \frac{dV_m(x, t)}{dt} \quad (13)$$

where C_m is the capacitance of the cell membrane in farads per micrometre squared, $r(x)$ is the radius of the neural process, and V_m is the membrane potential.

Kirchoff's law describes charge conservation, and Ohm's law makes the axial current proportional to the local voltage difference. Thus:

$$i_m(x, t) = -\frac{\partial i_{ax}(x, t)}{\partial x} = -g_{ax} \frac{\partial V_m(x, t)}{\partial x^2} \quad (14)$$

where i_{ax} denotes the axial current along the cell and g_{ax} is the axial conductance along the neuron measured in siemens micrometres. This equation connects the spatial pattern, more precisely the second spatial derivative of the membrane potential to the membrane current. Notice that this is the point where the viewpoint and the EC-IC sign convention was changed; negative membrane current causes positive inflection in the voltage.

Substituting eqns (14) and (13) back to eqn (12), we get the cable equation, where the capacitive and the resistive components are distinguished:

$$-g_{ax} \frac{\partial^2 V_m(x, t)}{\partial x^2} = 2\pi r(x) C_m \frac{dV_m(x, t)}{dt} + i_R(x, t) \quad (15)$$

Until this point, we have dealt with the relationship between the membrane current and the membrane potential measurable by intracellular electrodes. Now, we turn to the relationship between the membrane current and the extracellular potential generated by a neuron, with the intention to connect the intracellular and the extracellular potential measurements.

Considering the different units and the charge conservation, the membrane current calculated from the intracellular and the extracellular potentials are related as follows:

$$i_m(x, t) = I^{\text{siCSD}}(x, t) \times 2r(x) \quad (16)$$

where $r(x)$ is the diameter of the dendrite at position x .

From eqns 14 and 16, and assuming homogeneous intracellular fluid with σ_{IC} specific conductivity, the axial conductance $g_{ax} = \sigma_{IC} r^2 \pi$, thus:

$$\frac{\partial^2 V_m(x, t)}{\partial x^2} = -\frac{i_m(x, t)}{g_{ax}} = -\frac{2I^{\text{siCSD}}(x, t)}{\sigma_{IC} r(x)} \quad (17)$$

Integrating the two sides of eqn (17) with respect to space gives an equation for the distribution of the axial currents:

$$i_{ax}(x, t) = g_{ax} \frac{\partial V_m(x, t)}{\partial x} = i_{ax}(0, t) - \int_0^x 2r(x_1) \pi I^{\text{siCSD}}(x_1, t) dx_1 \quad (18)$$

where $i_{ax}(0, t)$ serves as the integral constant, also defining the boundary condition.

Assuming a sealed end:

$$i_{ax}(0, t) = 0 \quad (19)$$

This integral starts at the end of each neural branch ($x = 0$) where this boundary condition is given, proceeds towards the soma ($x = s$) and sums up at each branching point of the dendritic (or axonal) tree.

Thus, substituting eqn (19) into eqn (18) and integrating again both sides of eqn (18) shows that the membrane potential can be determined as:

$$V_m(x, t) = V_m(s, t) + \frac{2}{\sigma_{IC}} \int_s^x \int_0^{x_2} \frac{I^{\text{siCSD}}(x_1, t)}{r(x_1)} dx_1 dx_2 \quad (20)$$

Where $V_m(s, t)$, the somatic membrane potential, serves as a time-dependent spatial integrating constant. This time-dependent spatial baseline of the membrane potential is a piece of missing information from the EC potential; therefore, an IC membrane potential measurement is necessary at at least one site to provide this missing information and anchor the spatial distribution of the membrane potential at each time instance.

This second integral in eqn (20) starts at the soma where the boundary condition is given and goes through all branches of the neuron until all dendritic endings. The reverse direction of integration changes the sign in the equation. Although the siCSD values to be integrated are constant in each slice, different dendritic processes have different lengths and diameters in different slices. Thus, the results of the integration typically will be different for different dendritic branches, forming a specific 3D distribution in the whole dendritic tree.

Furthermore, the resistive part of the membrane current, accumulating all the channel currents, can be determined by using the reconstructed membrane

potential from eqn (20). Let us rewrite eqn (12) in current per surface units:

$$I_R(x, t) = I_m(x, t) - I_C(x, t) \quad (21)$$

Given that the time derivative of the reconstructed membrane potential from eqn (20) results in an estimate for the capacitive current, the resistive membrane current per unit membrane surface can be calculated as follows:

$$I_R(x, t) = I^{\text{siCSD}}(x, t) - C_m \frac{dV_m(x, t)}{dt} \quad (22)$$

Interestingly, here we obtain the resistive current, I_R , without using the membrane resistance, R_m , in either its passive or active (membrane potential- or synaptic activity-dependent) form.

The siCSD method takes into account the distance between the cell and the electrode, thus the I^{siCSD} is not proportional to the second spatial derivative of the EC potential, hence its second spatial integral does not correspond to the EC potential itself.

Testing the reconstruction on simulated data

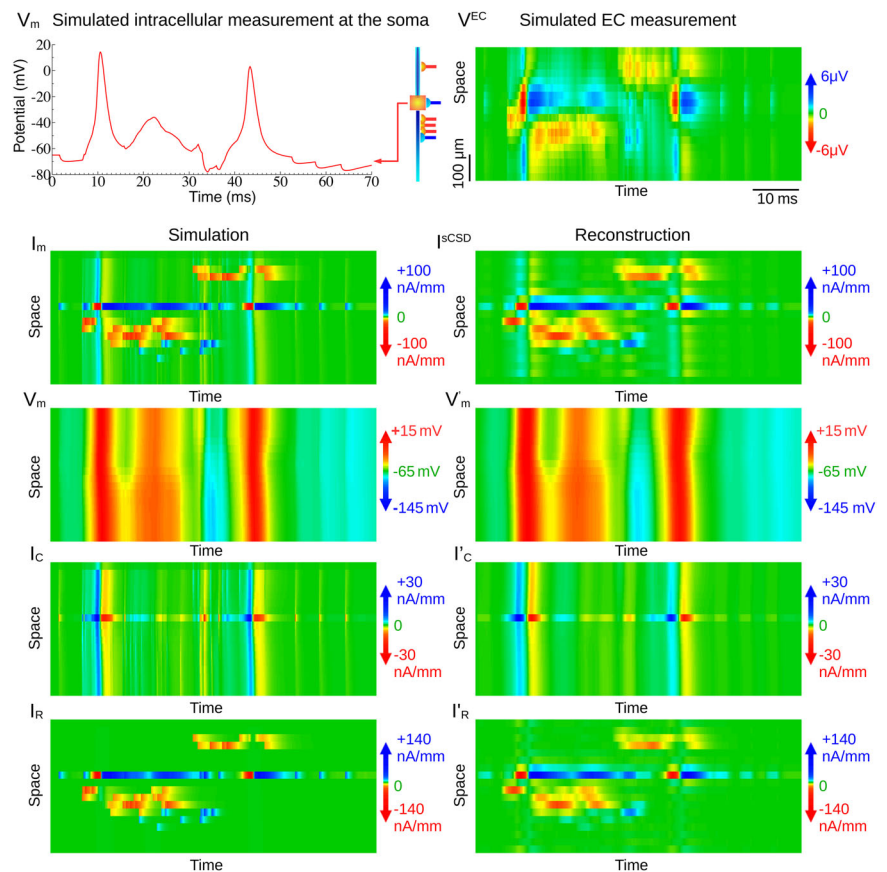
First, the membrane potential reconstruction was tested on a simulation of a simplified model of a neuron (Fig. 4).

The simulated neuron was a ball-and-stick type, which is consistent with the assumptions of the sCSD method. It had passive apical and basal dendrites, and a spherical soma equipped with active Hodgkin–Huxley-type Na^+ and K^+ channels. The activity was elicited by random initiation of excitatory alpha synapses located on the dendrites, and inhibitory synapses on the dendrites and on the soma. During the simulation time, 70 ms in duration, two large somatic spikes were generated by the model. The simulated EC measurements were calculated in a $50 \mu\text{m}$ distance on a virtual linear electrode array of 18 channels with $30 \mu\text{m}$ spatial resolution and were used to reconstruct the membrane potential together with the simulated V_m somatic membrane potential. In the first step, the net membrane current was estimated by applying the sCSD method, based on the V^{EC} alone.

The sCSD method approximates the neuron with a linear chain of point sources parallel to the electrode system and also estimates the cell–electrode distance, providing the first opportunity to verify the applicability and precision of the method. The time sample of the highest negative EC potential peak was chosen to estimate the cell–electrode distance, and the sCSD method resulted in a very precise estimation; the estimated distance was $49 \mu\text{m}$ and the real simulated distance was $50 \mu\text{m}$. Of

Figure 4. Simulated experiment to test the membrane potential reconstruction

First row, the data used for the reconstruction: simulated IC somatic membrane potential measurement (left) and simultaneous 18-channel extracellular potential (V^{EC}) measurement (right). Second row, comparison of the simulated (left) and reconstructed (right) net membrane current (I_m) source density. The net membrane current was determined by the spike current source density (sCSD) method, where the estimated cell electrode distance was $49 \mu\text{m}$, whereas the real simulation used $50 \mu\text{m}$. Note the counter-current system on the sides of each central source; the net membrane current for the whole neuron is zero in each time instance. Third row, spatial distribution of the simulated V_m (left) and reconstructed V'_m membrane potential (right). Fourth row, spatial distribution of the simulated (left) and reconstructed (right) capacitive membrane current components (I_C and I'_C). Fifth row, spatial distribution of the simulated (left) and reconstructed (right) pure resistive membrane current components (I_R and I'_R). Also note the disappearance of the counter-currents.



course, the distance estimation is not always as precise as in this case. A more thorough test of factors influencing the precision of distance estimation can be found in studies by Somogyvari et al. (2005, 2012).

Before the reconstruction, the mean of the net membrane current has been subtracted in each time instance, to ensure the zero sum of currents on the whole neuron.

In the second main step, the membrane potential was reconstructed by discrete integration, following eqn (20). Then the capacitive current was calculated by temporal derivation (eqn 13) and the resistive current by subtraction (eqns 21 and 22). All these reconstructed variables have been smoothed by calculating a 2.5-ms-long moving window average. For comparison, the resistive currents, the capacitive currents, the net membrane currents and the membrane potential were all saved from the NEURON simulations as ground-truth data.

As Fig. 4 shows, the whole simulated spatiotemporal membrane potential distribution was reconstructed with high precision based on the EC potential distribution and the assumed membrane potential measurement at the soma. The potential changes spread through the whole neuron in waves, and the distinct synaptic events melt together to form a spatially and temporally smoother membrane potential pattern. The figure also shows that the majority of the spatiotemporal variability in V_m belongs to the temporal variability of the baseline, measured by the IC electrode, and not to the spatial variability derived from the EC measurement. Thus, the incorporation of the IC membrane potential measurement was essential for a precise reconstruction in this case.

It should be noted that the degree of spatial uniformity or variability of the membrane potential depends on the morphology and on the electrical properties of the membrane and on those of the intracellular fluid.

The distinction between resistive and capacitive currents clearly shows different typical patterns of the two current types. The distribution of the capacitive current is rather stereotyped. A spatiotemporal wave of current is initiated at the sites of active synaptic currents or at the sites of voltage-sensitive currents and spreads through the cell, while active currents are more localized on the dendrites or at the soma. The CSD distribution inherits the properties of both currents, because all the localized active events are accompanied by spreading side waves of capacitive currents. In contrast, these side waves are markedly reduced on the reconstructed resistive membrane current maps.

In our second simulated example, the reconstruction was tested on a much more complex neuron model used by Hay et al. (2011). This neuron model not only uses the complex morphology of a thick-tufted layer 5b pyramidal neuron, but it is also equipped with active dendritic

Ca^{2+} and K^+ currents. The channel densities and the resulting complex dynamics were optimized to reproduce faithfully the parallel somatic and dendritic measurements of Larkum et al. (1999). After the 10 ms initial period of the 50-ms-long simulation, the activity was elicited by 10 randomly placed (alpha)synaptic current pulses on the dendrites. After the first somatic spike, the strong apical back-propagation initiated a long-lasting dendritic sink, which then generated two additional smaller somatic spikes (Fig. 5).

The corresponding EC potential was calculated at a spatial resolution of $50 \mu\text{m}$ along the cell, resulting in 29 channels of V^{EC} . From the 4260 compartments of the simulation, surface-weighted slice averages were calculated in 29 slices to serve as the ground truth for the comparison (Fig. 5, left column).

As a first step of the reconstruction, CSD distribution was calculated by the siCSD method, based on the V^{EC} and the known morphology of the neuron. The resulting spatiotemporal I^{siCSD} distribution closely followed the ground truth (Fig. 5, right column). The general structure of the reconstructed membrane potential, V'_m , resembles the ground-truth data, but some errors appear, especially during the periods of highly localized somatic activity. In the following steps, I'_C and I'_R were reconstructed and smoothed by a 0.75-ms-wide Gaussian kernel for comparison. The quality of the I_C and I_R reconstruction is similar; while the large structures follow the ground truth, the errors are inherited from the potential reconstruction to the capacitive and the resistive currents. Despite these errors, the correct conclusion can be drawn from the I_R map; the somatic spikes, the back-propagation and the long-lasting dendritic activities are all generated by active local resistive currents, in addition to the somatic after-hyperpolarization. In contrast, the large propagating dendritic source is missing from the I_R map, thus it is shown to be only a capacitive counter-current.

Besides the similarity of the spatiotemporal patterns, the quality of reconstruction has been evaluated by two different measures. The first one is the relative squared error (E_r):

$$E_r(I^{\text{CSD}}, I_m) = \frac{\sum_x (I^{\text{CSD}}(x, t) - I_m(x, t))^2}{\sum_x (I^{\text{CSD}}(x, t))^2 + \sum_x (I_m(x, t))^2} \quad (23)$$

where I_m denotes the ground-truth net membrane current, derived directly from the simulation, whereas I^{CSD} was determined by the sCSD method in the case of the ball-and-stick neuron or by the siCSD method for the Hay model, based on the calculated V^{EC} . This measure is between zero and two for each time point: zero if $I_m(t)$ and $I^{\text{CSD}}(t)$ are identical; one if one of them is negligible compared with the other; and two if they are

opposite. A similar relative error was calculated for all reconstructed variables: for the membrane potential V'_m , for the capacitive current I'_C and for the resistive current I'_R . The median and the median absolute deviation from the median of the momentary E_r over the whole length of the simulations are reported in Table 1.

Although the relative error is sensitive to the difference in amplitude between the ground truth and the reconstructed variable, the CSD analysis is often evaluated only qualitatively, by evaluating only the positions and the relative amplitudes of the sinks and sources. Furthermore, different CSD calculation methods can result in CSD distributions in different units: in amperes per metre cubed (tCSD), in amperes per metre squared (siCSD),

or in amperes per metre (sCSD). Therefore, in order to evaluate the similarity of the global CSD patterns (relative amplitudes) and to facilitate the comparison between different CSD methods, we introduced a second measure, the cosine similarity that is independent of the absolute amplitudes:

$$C(I^{\text{CSD}}, I_m) = \frac{\sum_{x,t} I^{\text{CSD}}(x,t) \times I_m(x,t)}{\sqrt{\sum_{x,t} (I^{\text{CSD}}(x,t))^2 \times \sum_{x,t} (I_m(x,t))^2}} \quad (24)$$

This C measure takes its value in the range of $[-1, 1]$: it is one if $I^{\text{CSD}} = a \times I_m$, thus the patterns are the same, but may be differently scaled; zero if I^{CSD} and I_m are orthogonal to each other; and minus one if they are

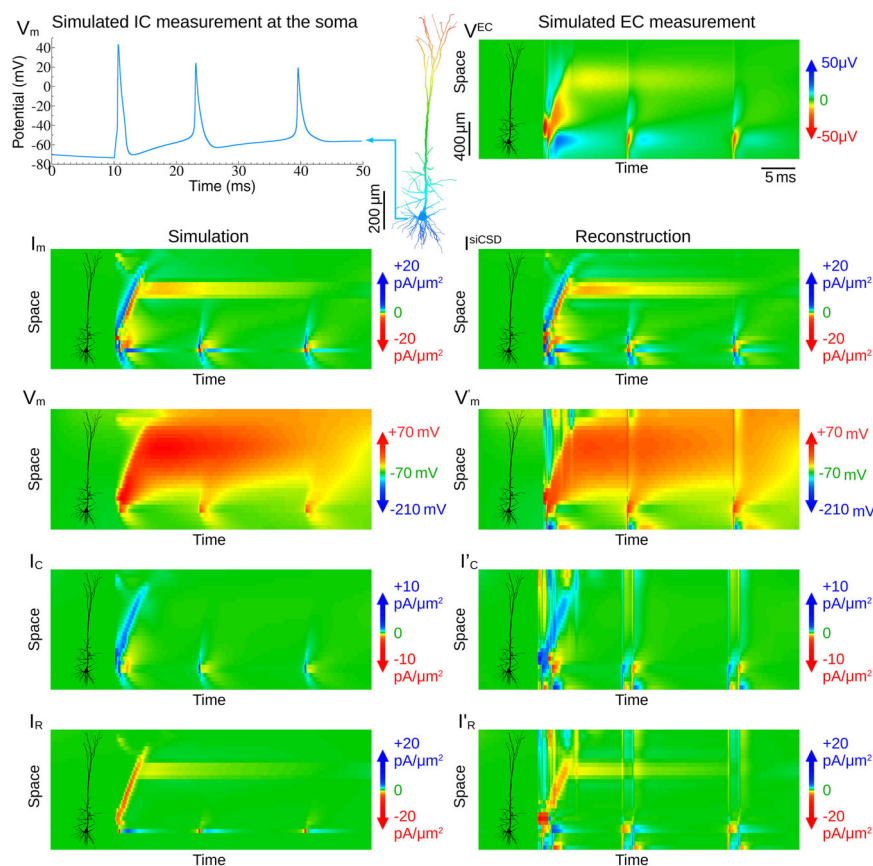


Figure 5. Simulated experiment designed to test the membrane potential

Reconstruction on a complex thick-tufted layer 5b neural model (Hay et al., 2011). First row, the data used for the reconstruction: simulated IC somatic membrane potential measurement (left) and simultaneous 29-channel extracellular potential (V^{EC}) measurement (right). Second row, comparison of the simulated (left) and reconstructed (right) net membrane current (I_m). The net membrane current was determined by the single-cell inverse current source density (siCSD) method, where the known morphology of the neuron was used. The first spike was elicited by 10 small synaptic events on the proximal and distal apical dendrites. The apical back-propagation initiated a long-lasting dendritic sink, which, in turn, generated two consecutive somatic spikes. The membrane potential (V'_m) reconstruction (right) followed the simulated (V_m) distribution (left) in general, but some errors appeared during large somatic activities. This is even more valid for the I'_C and I'_R distributions; the general structures were well reconstructed, but the errors were accumulated. Despite these errors, the correct conclusion can be drawn from the I_R map. The somatic spikes, the back-propagation and the dendritic activities are exhibited by active sinks, whereas the somatic after-hyperpolarization is caused by active sources.

Table 1. Reconstruction quality assessment for the two simulations: the simplified ball-and-stick neuron in Fig. 4 and the Hay model with complex morphology in Fig. 5

Parameter	Ball-and-stick neuron		Hay neuron	
	Median relative error \pm median absolute deviation	Cosine similarity	Median relative error \pm median absolute deviation	Cosine similarity
I_m	0.09 ± 0.07	0.89	0.06 ± 0.04	0.8
V_m	0.0001 ± 0.0001	0.999	0.002 ± 0.002	0.98
I_C	0.1 ± 0.08	0.827	0.06 ± 0.05	0.49
I_R	0.09 ± 0.08	0.879	0.05 ± 0.03	0.47
tCSD	0.15 ± 0.003	0.86	0.34 ± 0.07	0.63

The relative squared error is sensitive to the difference in amplitude between the ground truth and the reconstruction, whereas the cosine similarity is independent of the absolute amplitudes, because it evaluates only the similarity of the relative amplitudes. For the simplified morphology, the membrane current (I_m) was estimated by the sCSD method, but for the complex morphology of the Hay model, I_m was estimated by the siCSD method. In both cases, the CSD estimation was more precise than the traditional CSD (tCSD). We would like to emphasize here that the membrane potential (V_m) reconstruction was very precise in both cases, and all the other variables were determined with reasonable precision.

opposite. Cosine similarity was calculated in a similar manner between all the reconstructed variables and the corresponding ground-truth data.

Table 1 shows the evaluation of the reconstruction qualities for all the determining variables and for both neuron simulations. The momentary relative error (E_r) of sCSD and tCSD has been compared by Wilcoxon signed rank test ($n = 560$ time samples): the sCSD produced significantly lower error, with $z = -2.32$, $P = 0.0101$. The membrane potential (V_m) reconstruction was almost perfect, but the capacitive (I_C) and especially the resistive (I_R) current could have been determined less precisely. For the Hay model, the siCSD method resulted in significantly lower estimation error compared with the tCSD method (Wilcoxon signed rank test, $n = 993$ time samples, $z = -27.3$, $P \approx 0$). All the investigated variables were reconstructed with slightly lower relative error than in the ball-and-stick case, but the lower cosine similarity shows differences in the patterns. Based on multiple similar simulations, we conclude that our method is able to reconstruct the spatiotemporal distribution of the membrane potential of the neuron precisely. Furthermore, the decomposition of the net membrane current into resistive and capacitive components results in less precise but qualitatively adequate estimations.

Application to *in vitro* measurements

Here, we demonstrate the practical application of the membrane potential reconstruction method on paired intracellular and extracellular recordings of a CA1 pyramidal neuron *in vitro* (Fig. 6). In simulations, it is ensured that the EC potential is generated by the simulated neuron itself. However, this is not the case for real

measurements, where the signals generated by multiple neurons are mixed on the EC electrode. Therefore, after recording the spontaneous activity of the neuron (Fig. 6A), 750 action potentials were collected (Fig. 6B), and the IC STA was calculated both for IC (Fig. 6C) and EC potentials (Fig. 6F, top graph) in 29 channels separately. Note that this practically is a supervised process; no spike sorting was necessary because the IC recording provided the ground truth for the timing of the action potentials (Fig. 6D). In this manner, it was possible to determine the EC action potential pattern of the real neuron, even if its amplitude was so low ($11 \mu V$), that it would not have been possible to perform a blind, or unsupervised, spike sorting on the raw EC signal itself.

Reconstruction of the membrane potential

Figure 6E shows the morphology of the neuron and the relative position of the electrode contact points. This method results in the same number of slices as electrodes. The contact points and the corresponding slices of the neuron are represented using the same colour. The columns in Fig. 6F and G show the steps and the results of the reconstruction in two forms: in Fig. 6F, coloured lines correspond to the electrode or cell slice of the same colour (in Fig. 6E), whereas in Fig. 6G, potential and current distributions are represented in spatiotemporal maps, where the colours were chosen relative to the amplitude. The first and second rows in Fig. 6F and G show the STA V^{EC} and the calculated siCSD distribution, respectively, and the third row shows the reconstructed membrane potential distribution.

Although the initiation and propagation are also observable on the reconstructed membrane potential, the

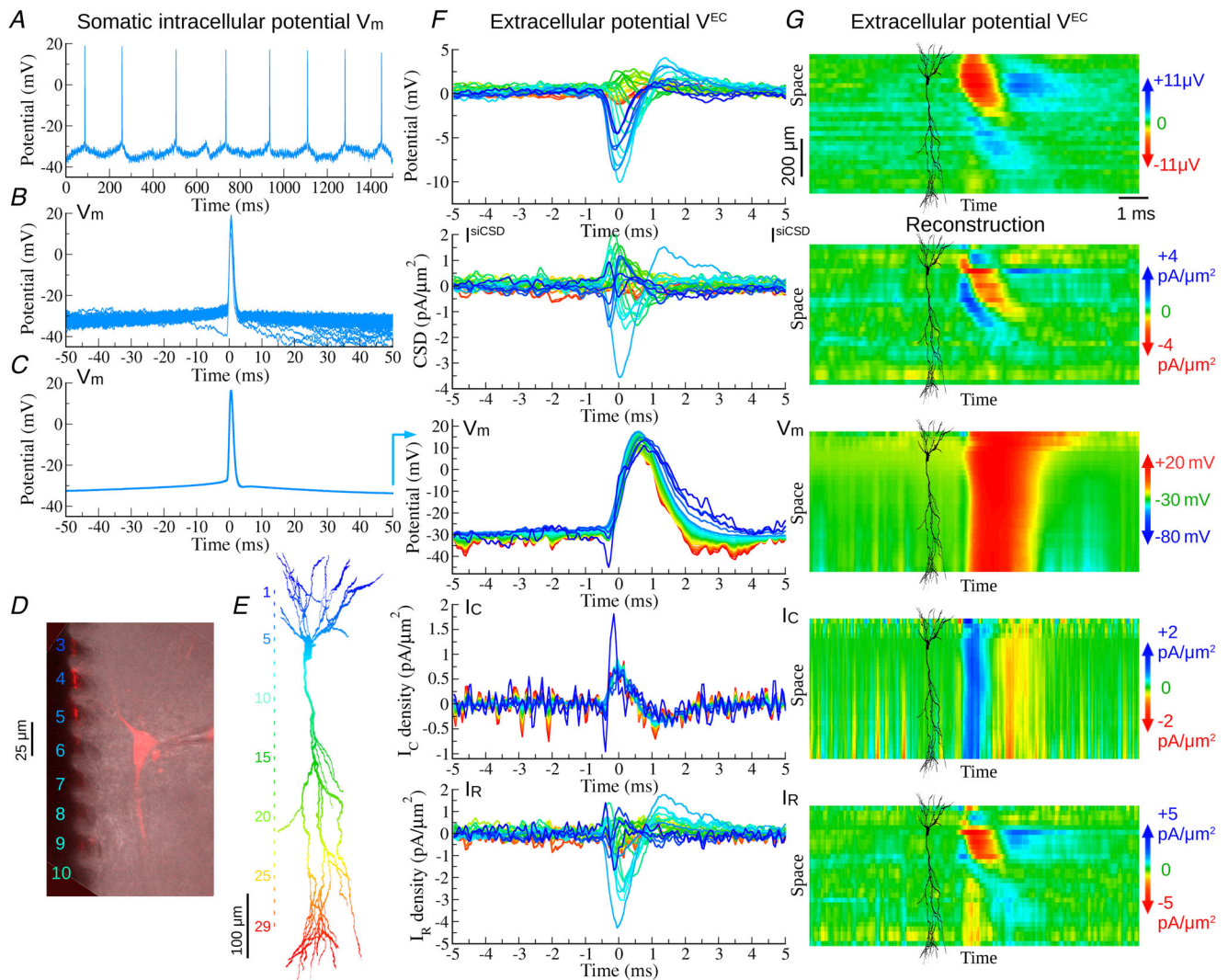


Figure 6. Membrane potential reconstruction based on parallel extracellular and intracellular measurements

A, an example of the intracellular membrane potential (V_m) trace from a CA1 pyramidal neuron. **B**, examples from the detected spikes. **C**, the mean of the 750 detected membrane potential traces in a 100-ms-long time window around the 0 mV threshold crossing times. Only a 10 ms interval was used for the membrane potential reconstruction. **D**, fluorescent imaging of the cell. The extracellular (EC) electrode contact sites are shown on the left (black, with coloured labels for the corresponding channel numbers); and the patch-clamped cell filled with Alexa 594 (red) and its corresponding micropipette are shown on the right side. **E**, Neurolucida reconstruction of the cell, parallel to the 29 used contact sites of the electrode with 25 μm spacing. The extracellular contact sites, the corresponding slices of the cell and the curves in **F** are coloured according to their spatial positions. **F**, the steps of the reconstruction from the top: the measured spike-triggered mean EC potential; the calculated single-cell inverse current source density (siCSD); the reconstructed membrane potential, V_m ; the capacitive current, I_c , and the resistive current, I_r . **G**, same as **F**, but represented as spatiotemporal heatmaps. The end of the colour scale corresponds to the absolute amplitude maxima in the subgraphs in **F**. The main negative deflection of V^{EC} around the soma is accompanied by a secondary one around the distal apical region. The siCSD map clearly shows an initial sink on the basal fourth to fifth channels, followed by the largest sink on the soma located at the sixth channel. The action potential back-propagation is traceable up to 10 channels on the apical dendrite. The reconstructed V_m exhibited slight depolarization before the action potential initialization at the basal and somatic region. The rising phase of the action potential was observable at multiple parallel sites, but V_m is rather homogeneous throughout the neuron and drops only 20% while travelling through the apical dendrite. The reconstructed resistive current shows early sinks near the soma, reduced counter-currents (compared with the CSD), active sinks along the distal apical dendrites, and back-propagation on the apical trunk.

whole V_m pattern was surprisingly compact along the neuron. The observable time delays in action potential propagation between the different parts of the neuron were smaller than the whole length of the action potential, thus the potential peak was present at almost the same time all along the neuron. Furthermore, the amplitude of the action potential dropped only 20% until it reached the apical dendrites, so V_m is mostly homogeneous throughout the neuron. This observation agrees with our test simulations (Fig. 4) and underlines that the integration constant is the dominant contributor to the membrane potential, and it cannot be neglected. Focusing on the lower-amplitude events preceding the onset of the action potential, our reconstruction shows that the depolarization was higher in the region of the basal dendrites than in the rest of the neuron before the spike initialization (Fig. 6F, V_m , blue lines), although fluctuating depolarization occurred in the distal apical dendrites as well.

Zooming into the initiation of the action potential (Fig. 7), it is clear that the depolarization occurred at three distinct sites at the same time: in the basal region where the axon is located, in the perisomatic region, and in the far apical dendritic region. Following this multi-site initialization, this depolarization propagated from the initial points in both basal and apical directions. We can assume that the perisomatic region, including the axon initial segment and the more basal region that includes the first nodes of Ranvier of the axon, contained voltage-sensitive channels in high density, thus exhibiting

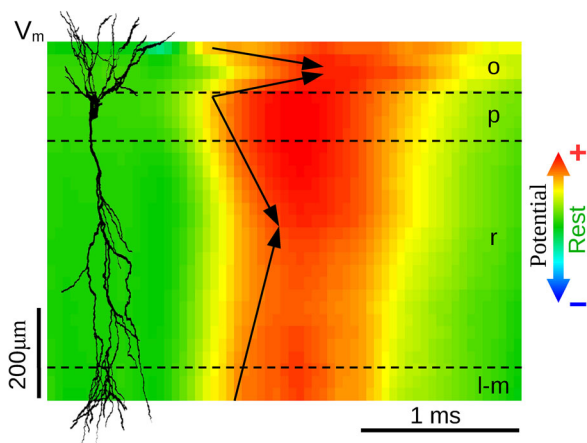


Figure 7. Multi-site initiation of the action potential

Depolarization became apparent at distinct dendritic sites at the same time: in the basal region where the axon is located, in the perisomatic region and in the distal apical dendritic region. After the multi-site initiation, depolarization propagated in both apical and basal directions. Dashed lines denote the borders of the hippocampal layers. Abbreviations: l-m, stratum lacunosum-moleculare; o, stratum oriens; p, stratum pyramidale; r, stratum radiatum.

a low threshold and early depolarization. On the other side, the distal apical dendrites are much thinner than the proximal part, thus they can be more sensitive to the influx of positive charges compared with the region of the trunk.

The net membrane current was decomposed into capacitive and resistive components with the help of the reconstructed V_m (Fig. 6F and G, fourth and fifth rows). During the action potential, the reconstructed resistive current, which consists of all passive and active conductances, builds up from three major inward components, all of which have their assumptive roles in the action potential generation: a dominant contribution at the level of soma that propagates back to the apical trunk; some very well-localized components in the basal region, presumably corresponding to the axon initial segment and the nodes of Ranvier; and a more distributed current along the apical dendritic axis.

The siCSD method determines a laminar CSD distribution on the 3D morphology of the neuron, based on the V^{EC} potential measured only in the locations of the EC electrode system, on 29 electrodes in the actual case. However, the EC potential can be recalculated in any other location around the neuron, based on the estimated CSD distribution using the T transfer matrix (eqn 9) for the new locations. This procedure can be considered as a spatial extrapolation of the V^{EC} , because it is equal to the measured V^{EC} in the electrode locations and provides an estimation everywhere else.

Although the determined CSD distribution is laminar, according to the assumption of the siCSD method, this does not hold for the reconstructed membrane potential. Given that the different dendritic processes have different lengths and diameters in different slices, the reconstructed membrane potential, hence the capacitive and the resistive currents, are typically different in distinct dendritic branches. In order to obtain a full picture of the relationship between the EC potential and the membrane currents and potential, the 3D distribution of I^{siCSD} , V_m and I_R are shown in Fig. 8, along with the whole dendritic tree in the different phases of action potential generation, parallel to the estimated V^{EC} around the neuron. This comparison shows specific phase relationships between these variables: V^{EC} and the CSD reach their negative peak amplitude at $t = 0$ ms, when the V_m traverses the 0 mV threshold. In contrast, V_m reaches its peak at $t = 0.5$ ms, by the time when V^{EC} is greatly reduced. Interestingly, both the basal and the apical I_R density shows large inward currents at $t = -0.25$ ms, preceding the V^{EC} and CSD amplitude peaks. This current was masked by the outward counter-currents of the somatic sinks on the CSD map.

An animation related to Fig. 8, showing all phases of the action potential generation, is available here:

- <https://youtu.be/VdF30RfdOLg>

Discussion

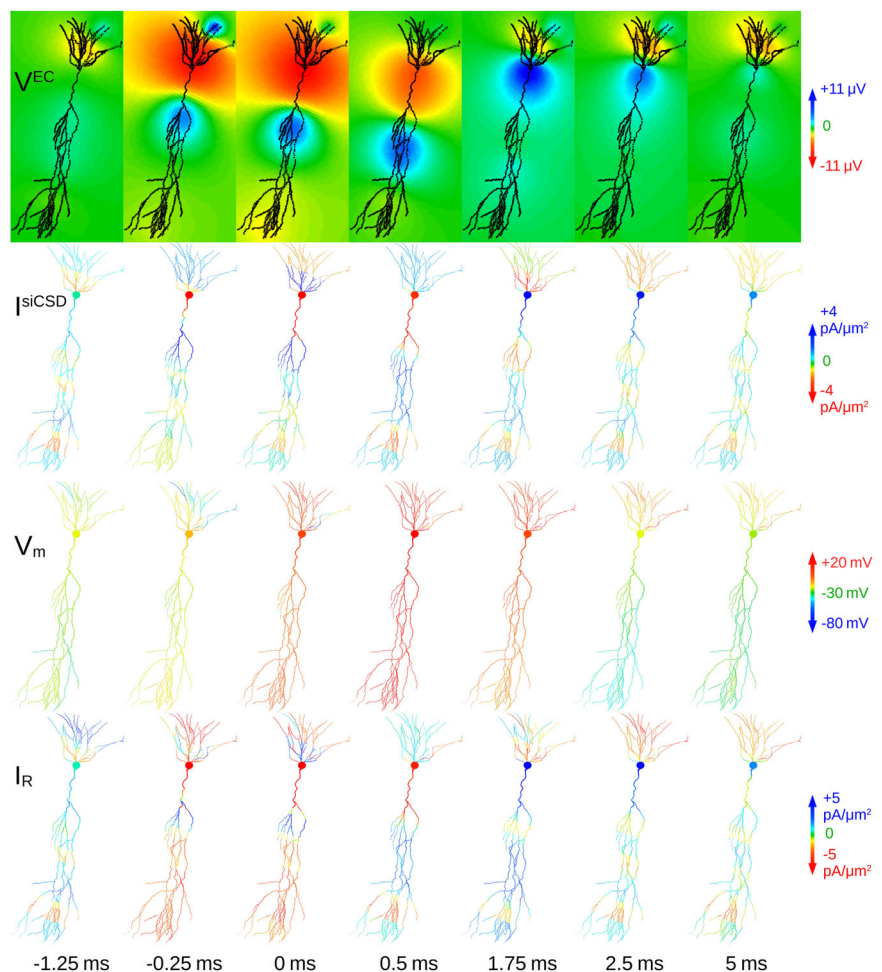
The interpretation of current sinks and current sources is often oversimplified in the physiological literature. Sinks are mostly considered as signs of depolarization, whereas sources refer to the counter-currents or are associated with the hyperpolarization of the membrane. However, the momentary zero sum of the CSD is a warning sign of this oversimplification, because both the depolarizing and the hyperpolarizing synaptic currents result in the same amount of sinks and sources on the CSD maps. Furthermore, the counter-currents (i.e. the accompanying sources around an active sink) are the EC signs of the spreading depolarization in the IC volume. Figure 2 shows that a local sink can be a sign either of local depolarization or of remote hyperpolarization spreading to the position, and, in a similar manner, a local source can be a sign either of local hyperpolarization or of remote depolarization spreading to the local position.

The membrane potential reconstruction presented here allowed the distinction of the resistive and capacitive currents, thus allowing a more precise interpretation of

the observed currents. The different properties of the resistive membrane current distribution and the CSD are emphasized here. Given that the CSD is the density of the net membrane current, the sum of the CSD along a whole intact cell should be zero at each moment in time according to the charge conservation. In contrast, the sum of the resistive current is not necessarily zero, and it governs the membrane potential dynamics. A rather surprising conclusion arises from these properties, which is that a spherically symmetric or spatially clamped neuron does not generate any EC potential during resting states or during generation of an action potential. While symmetric resistive currents pass through the membrane and the membrane potential changes steeply, the capacitive current counterbalances it perfectly, and there will be no detectable change in the EC potential. The spatial extension and electric inhomogeneity of the neuron are necessary to generation of the EC potential, thus in the original experiments of Hodgkin and Huxley there were no EC potential changes, and only the IC potential changed. From a modelling point of view, this means that a single compartmental neuron model cannot

Figure 8. Spatiotemporal distribution patterns along a complete neuron morphology

Estimated spatiotemporal distributions of the extracellular potential (V^{EC}), the corresponding current source density distribution estimated by the single-cell inverse current source density method ($siCSD$), the membrane potential (V_m) and resistive current (I_R) on the same neuron. Time is relative to the zero threshold crossing of the somatic V_m . Note the uneven time intervals between the consecutive snapshots. Although the current source density (CSD) distribution is strictly laminar owing to the assumptions of the single-cell inverse current source density ($siCSD$) method, this does not hold for the membrane potential or for the resistive current. The presented variables show clear phase shifts: the dendritic I_R peaks at $t = -0.25$ ms; V^{EC} , $siCSD$ and the somatic I_R reach their (negative) peaks at $t = 0$; and V_m peaks at $t = 0.5$ ms.



be used to model the EC potential, owing to the zero net current (Chizhov et al. 2015; Einevoll et al. 2013).

Our membrane potential reconstruction procedure does not require either the modelling of channel dynamics or the setting of specific channel conductances. The currents resulting from these conductances are already included in the measured EC potential in the form of the calculated CSD. Besides the morphology and the spatial position of the neuron relative to the electrode array, the only passive electrical parameters required for the reconstruction of the membrane potential are the specific membrane capacitance (C_m) and the specific conductances of the intracellular (σ_{IC}) and extracellular (σ_{EC}) fluids.

Both σ_{EC} (Ness et al., 2015; Varona et al., 2000) and C_m (Gentet et al., 2000) are relatively well-known parameters. However, the values of the specific resistivity of the intracellular cytoplasm scatter more in the literature: Chitwood et al. (1999) found values close to 200 Ω cm, for CA3 pyramidal neurons (and admitted that their resolution was not sufficient to draw conclusions), whereas Stuart and Spruston (1998) suggested 70–100 Ω cm for L5 neurons, Foster et al. (1976) reported 40 Ω cm as the mean for the *Aplysia* giant axon, but found individual neurons with as low as 11 Ω cm. In the simulated tests, we used values of 100 or 123 Ω cm both during the simulations and during the reconstruction, but for the measured hippocampal neuron, we could not rely on such ground-truth data. Interestingly, σ_{IC} determines the ratio of the IC and EC contribution to the full V_m distribution in eqn (20). This means that the physiological constraints, including the fact that V_m cannot exceed the equilibrium potential of Na^+ in the positive direction or the equilibrium potential of K^+ in the negative side, set a lower bound for σ_{IC} or, equivalently, higher bound for the resistivity. In our case, we had to set it as low as 17 Ω cm = 6×10^{-6} S μm^{-1} to avoid exceeding these physiological ranges.

Previous studies have attempted to bridge the gap between the EC and the IC potentials at the neural population scale. Gratiy et al. (2011) aimed to distinguish between different synaptic components on neocortical neuron populations, underlying an evoked potential in a cortical column. Three neuron populations were included: a layer 2/3 small pyramidal, a layer 4 spiny stellate and a layer 5 large pyramidal cell population. Their strategy was to model the depth profile of the evoked CSD distribution and the subsequent depth profile of the LFP, evoked by localized synaptic inputs. This process is equal to solving the forward model. Then, the inverse problem has been solved, by matrix inversion, back-transforming the LFP to synaptic activations on their neural populations. However, several obstacles appeared in avoiding the calculation of the inverse solution. After the inverse transformation, all the calculated synaptic profiles had zero mean, even if the original synaptic input did not. This means that

the forward transformation projected the problem into a zero-mean subspace, preventing the correct inversion of the profiles. To overcome the problem and to find a unique solution, the inputs were restricted to be excitatory only.

Chizhov et al. (2009, 2015) took a different approach. They identified that the 1D traditional CSD is proportional to the second spatial derivative of the EC potential (eqn 3) and it is also proportional to the second spatial derivative of the IC membrane potential, according to the cable equation (eqn 15). However, they concluded erroneously that the proportionality of the second spatial derivatives also implies the proportionality of the EC and IC potentials. Their approach neglected the time-dependent constant of integration, which, as our results showed, cannot be neglected.

In this work, we demonstrate that the zero-space problem defined by Gratiy et al. (2011) and the integration constant missing from the calculations of Chizhov et al. (2009) are two facets of the same problem: the EC potential pattern by itself does not contain enough information to reconstruct the single-cell IC membrane potential based only on EC measurements.

Hamilton et al. (2018) have applied an interesting new strategy, called model assimilation, to approximate the IC membrane potential based on the EC measurements. They used only one intracellular and one extracellular channel. Their method starts with an approximate model of the system and an assumptive observation function, neither the model nor the observation function need to be accurate in the beginning. Then, the non-linear Kalman filter-based model assimilation allows for the development of both the model and the observation function to be more and more precise by predicting the next observation and ameliorating the model and the observation function in alternating steps. Particularly, in the work of Hamilton et al. (2018), the initial model describing the intracellular dynamics is the Fitzhugh–Nagumo model, while the observation function leading to the extracellular potential has been approximated by the time derivative of the intracellular membrane potential. Although it is promising that intracellular dynamics could be approximated in this way to some extent, they did not attempt to reconstruct the spatial distribution of the membrane potential or the inputs to the neuron. At this point, it is not clear whether this method could handle the missing information caused by the zero space problem.

Considering the state-of-the-art experimental electrophysiology literature, these measurements are still posing long-standing challenges, and there have been only a few successful published attempts where researchers were able to obtain IC–EC paired data from single neurons. In their early pioneering study, Freygang and Frank (1959) started to record simultaneous signals inside and outside the soma of a motor neuron in order to

estimate the relationship between intra- and extracellular waveforms. Wehr et al. (1999) were the first to use a metal electrode in simultaneous recordings; however, the classical study from the Buzsáki laboratory, conducted by Henze et al. (2000), became the most widespread because they provided the first *in vivo*, open-source ground-truth dataset using tetrodes and sharp glass micropipettes with reconstructed cell morphology included. Anastassiou et al. (2015) were the first to use multichannel silicon probes in colocalized and simultaneous recordings. In the most recent study, Buccino et al. (2022) combined patch-clamp and planar two-dimensional, high-density multi-electrode array (MEA) recordings and also performed cell morphology reconstruction; however, they obtained their data from embryonic rat cell culture.

Although it would be very promising to apply our membrane potential reconstruction method *in vivo* and attempt to identify the synaptic currents during functioning in the brain, until now only two groups (led by Adam Kampff, UCL, and Ed Boyden, MIT) have been able to record high-density, simultaneous IC–EC data *in vivo*, but they have been mainly restricted to recording juxtacellular or ‘loose-patch’ configurations instead of whole-cell patch clamp, and none of them has included detailed morphological information in their dataset (Allen et al., 2018; Marques-Smith et al., 2018; Neto et al., 2016).

There are multiple other limitations that could arise but are not discussed in detail here. These can include the following. The considerably large shank of an inserted EC probe might cause tissue distortion and unwanted cell damage in its closest vicinity, making it extremely difficult to access surrounding intact cells. In contrast, the micropipette can break easily when getting close enough to the EC electrode array. Finally, owing to the proximity of the two electronic systems, recorded signals might even interfere, resulting in additional noise or cross-talk artefacts.

In terms of functional optical imaging, advanced techniques are rapidly evolving, but they also have several drawbacks. In addition to their still insufficient spatial and temporal resolution, functional imaging faces limitations regarding its sensitivity and photostability that might hinder the proper observation of fine-scaled intracellular events from the extracellular space. The most recent Ca^{2+} indicators are able to achieve single-spike sensitivity (earlier ones were not as precise), but they only provide the readout of above-threshold events (action potentials) owing to the indirect, proxy nature of intracellular Ca^{2+} dynamics (Zhang et al., 2021). Although membrane voltage imaging is capable of monitoring even subthreshold intracellular oscillations and seems to have sufficiently fast temporal kinetics, its robustness is not yet sufficiently optimized for prolonged photostability and biocompatibility, because early saturation or rapidly increased photobleaching effects have been

widely reported (Bando et al., 2019). Furthermore, various aberrant activity patterns have also been revealed in these genetically modified animal strains (Miyashita et al., 2013; Steinmetz et al., 2017). Other disadvantages of imaging techniques include limited penetrating ability, because deeper subcortical structures (e.g. the hippocampus, the basal ganglia or the brainstem nuclei) remained very difficult to access *in vivo*, especially in larger species, such as non-human primates. Lastly, it has to be mentioned that the deconvolution of realistic membrane potential changes from the detected (relative) fluorescence intensities remains non-trivial or sometimes unfeasible owing to the contamination by densely overlapping cells, different time scales, stochastic kinetics of the fluorescence signals or increased background autofluorescence (Bando et al., 2019; Harris et al., 2016).

A limitation of our method comes from the fact that the reconstruction requires a clear identification of the EC potentials caused by the neuron. Although the applied STA assures that only EC potentials that are strictly correlated with the action potential generation of the neuron contribute significantly to the mean, some contributions from the correlated network activity cannot be excluded completely. The STA in such a short time window allowed the determination of the spike-related active currents that strictly precede or follow the action potential generation. This allowed the demonstration of our reconstruction method. However, synaptic currents that made the given cell fire are presumed to act on a longer time scale. Determination of the synaptic currents on a longer time scale makes the distinction between correlated network effects and the EC potential generated by the recorded neuron rather challenging.

Tests on simulations with complex neuronal morphologies showed that the laminar CSD approximation of the siCSD method can cause a relatively large error in the reconstruction. Owing to the radial distribution of the basal dendrites on the simulated layer 5b neuron, the thin slice of the soma also contains a significant number of dendrites. Thus, the determined CSD for this slice will differ from the CSD on the soma alone. After the second integration, when the soma is set to the potential level of the IC measurement, this difference can cause a shift in the V_m level of the whole neuron. However, this effect is negligible for the ball-and-stick neuron and for our reconstructed CA1 neuron owing to the more axial directions of the basal dendrites.

Most of our knowledge accumulated on neural coding is based on EC measurements, where only the outputs of the neurons are observable in the form of EC spikes. Although we presented our combined experimental and computational findings focusing on the fine details of action potential generation and propagation along the entire neuronal axis, in a broader perspective our

reconstruction method could be an efficient tool for localizing synaptic input currents, which represent the active causes of intricate spatiotemporal changes of the membrane potential that eventually lead to spike generation. This might lead to a deeper understanding of the input–output transformation implemented by the neurons and of the subcellular biophysics of neural computation.

References

- Allen, B. D., Moore-Kochlacs, C., Bernstein, J. G., Kinney, J. P., Scholvin, J., Seoane, L. F., Chronopoulos, C., Lamantia, C., Kodandaramaiah, S. B., Tegmark, M., & Boyden, E. S. (2018). Automated in vivo patch-clamp evaluation of extracellular multielectrode array spike recording capability. *Journal of Neurophysiology*, **120**(5), 2182–2200.
- Anastassiou, C. A., Perin, R., Buzsáki, G., Markram, H., & Koch, C. (2015). Cell type- and activity-dependent extracellular correlates of intracellular spiking. *Journal of Neurophysiology*, **114**(1), 608–623.
- Bando, Y., Sakamoto, M., Kim, S., Ayzenshtat, I., & Yuste, R. (2019). Comparative evaluation of genetically encoded voltage indicators. *Cell Reports*, **26**(3), 802–813.e4.
- Buccino, A. P., Damart, T., Bartram, J., Mandge, D., Xue, X., Zbili, M., Günswein, T., Jaquier, A., Emmenegger, V., Markram, H., Hierlemann, A., & Van Geit, W. (2022). A multi-modal fitting approach to construct single-neuron models with patch clamp and high-density microelectrode arrays. *bioRxiv*. 502468.
- Buzsáki, G. (2004). Large-scale recording of neuronal ensembles. *Nature Neuroscience*, **7**(5), 446.
- Buzsáki, G., Anastassiou, C. A., & Koch, C. (2012). The origin of extracellular fields and currents–EEG, ECoG, LFP and spikes. *Nature Reviews Neuroscience*, **13**(6), 407.
- Carnevale, N. T., & Hines, M. L. (2006). *The NEURON book*. Cambridge University Press.
- Chitwood, R., Hubbard, A., & Jaffe, D. (1999). Passive electrotonic properties of rat hippocampal CA3 interneurons. *The Journal of Physiology*, **515**(3), 743–756.
- Chizhov, A. V., Pokrovskii, A. N., Terry, J., & Sargsyan, A. (2009). Estimation of synaptic currents by recordings from extracellular electrodes. *Biofizika*, **54**, 495–499.
- Chizhov, A. V., Sanchez-Aguilera, A., Rodrigues, S., & Menendez de la Prida, L. (2015). Simplest relationship between local field potential and intracellular signals in layered neural tissue. *Physical Review E*, **92**(6), 1–9.
- Cserpán, D., Meszéna, D., Wittner, L., Tóth, K., Ulbert, I., Somogyvári, Z., & Wójcik, D. K. (2017). Revealing the distribution of transmembrane currents along the dendritic tree of a neuron from extracellular recordings. *eLife*, **6**, e29384.
- Einevoll, G. T., Kayser, C., Logothetis, N. K., & Panzeri, S. (2013). Modelling and analysis of local field potentials for studying the function of cortical circuits. *Nature Reviews Neuroscience*, **14**(11), 770.
- Foster, K. R., Bidinger, J. M., & Carpenter, D. O. (1976). The electrical resistivity of cytoplasm. *Biophysical Journal*, **16**(9), 991–1001.
- Freygang, W., & Frank, K. (1959). Extracellular potentials from single spinal motoneurons. *The Journal of General Physiology*, **42**(4), 749–760.
- Gentet, L. J., Stuart, G. J., & Clements, J. D. (2000). Direct measurement of specific membrane capacitance in neurons. *Biophysical Journal*, **79**(1), 314–320.
- Gidon, A., Zolnik, T. A., Fidzinski, P., Bolduan, F., Papoutsis, A., Poirazi, P., Holtkamp, M., Vida, I., & Larkum, M. E. (2020). Dendritic action potentials and computation in human layer 2/3 cortical neurons. *Science*, **367**(6473), 83–87.
- Gratiy, S. L., Devor, A., Einevoll, G. T., & Dale, A. M. (2011). On the estimation of population-specific synaptic currents from laminar multielectrode recordings. *Frontiers in Neuroinformatics*, **5**, 32.
- Hajos, N., Ellender, T. J., Zemankovics, R., Mann, E. O., Exley, R., Cragg, S. J., Freund, T. F., & Paulsen, O. (2009). Maintaining network activity in submerged hippocampal slices: Importance of oxygen supply. *European Journal of Neuroscience*, **29**(2), 319–327.
- Hamilton, F., Berry, T., & Sauer, T. (2018). Tracking intracellular dynamics through extracellular measurements. *PLoS One*, **13**(10), e0205031.
- Harris, K. D., Quiroga, R. Q., Freeman, J., & Smith, S. L. (2016). Improving data quality in neuronal population recordings. *Nature Neuroscience*, **19**(9), 1165.
- Hay, E., Hill, S., Schürmann, F., Markram, H., & Segev, I. (2011). Models of neocortical layer 5b pyramidal cells capturing a wide range of dendritic and perisomatic active properties. *PLoS Computational Biology*, **7**(7), e1002107.
- Henze, D. A., Borhegyi, Z., Csicsvari, J., Mamiya, A., Harris, K. D., & Buzsáki, G. (2000). Intracellular features predicted by extracellular recordings in the hippocampus in vivo. *Journal of Neurophysiology*, **84**(1), 390–400.
- Hodgkin, A. L., & Huxley, A. F. (1952). A quantitative description of membrane current and its application to conduction and excitation in nerve. *The Journal of Physiology*, **117**(4), 500–544.
- Kerekes, B. P., Tóth, K., Kaszás, A., Chiovini, B., Szadai, Z., Szalay, G., Pálfi, D., Bagó, A., Spitzer, K., Rózsa, B., Ulbert, I., & Wittner, L. (2014). Combined two-photon imaging, electrophysiological, and anatomical investigation of the human neocortex in vitro. *Neurophotonics*, **1**(1), 011013.
- Kumar, S. S., Günswein, T., Buccino, A. P., Xue, X., Bartram, J., Emmenegger, V., & Hierlemann, A. (2022). Tracking axon initial segment plasticity using high-density microelectrode arrays: A computational study. *Frontiers in Neuroinformatics*, **16**, 957255.
- Larkum, M. E., Zhu, J. J., & Sakmann, B. (1999). A new cellular mechanism for coupling inputs arriving at different cortical layers. *Nature*, **398**(6725), 338–341.
- Lindén, H., Hagen, E., Leski, S., Norheim, E. S., Pettersen, K. H., & Einevoll, G. T. (2014). LFPy: a tool for biophysical simulation of extracellular potentials generated by detailed model neurons. *Frontiers in Neuroinformatics*, **7**, 41.

- Marques-Smith, A., Neto, J. P., Lopes, G., Nogueira, J., Calcaterra, L., Frazão, J., Kim, D., Phillips, M. G., Dimitriadis, G., & Kampff, A. (2018). Recording from the same neuron with high-density CMOS probes and patch-clamp: A ground-truth dataset and an experiment in collaboration. *bioRxiv*, 370080.
- Meszéna, D., Kerekes, B. P., Pál, I., Orbán, G., Fiáth, R., Holzhammer, T., Ruther, P., Ulbert, I., & Márton, G. (2019). A silicon-based spiky probe providing improved cell accessibility during in vitro slice recordings. *Sensors and Actuators B: Chemical*, **297**, 126649.
- Miyashita, T., Shao, Y. R., Chung, J., Pourzia, O., & Feldman, D. (2013). Long-term channelrhodopsin-2 (ChR2) expression can induce abnormal axonal morphology and targeting in cerebral cortex. *Frontiers in Neural Circuits*, **7**, 8.
- Ness, T. V., Chintaluri, C., Potworowski, J., Leski, S., Glabska, H., Wojcik, D. K., & Einevoll, G. T. (2015). Modelling and analysis of electrical potentials recorded in microelectrode arrays (MEAs). *Neuroinformatics*, **13**(4), 403–426.
- Neto, J. P., Lopes, G., Frazão, J., Nogueira, J., Lacerda, P., Baião, P., Aarts, A., Andrei, A., Musa, S., Fortunato, E., & Barquinha, P. (2016). Validating silicon polytrodes with paired juxtacellular recordings: method and dataset. *Journal of Neurophysiology*, **116**(2), 892–903.
- Nicholson, C., & Freeman, J. A. (1975). Theory of current source-density analysis and determination of conductivity tensor for anuran cerebellum. *Journal of Neurophysiology*, **38**(2), 356–368.
- Pettersen, K. H., Devor, A., Ulbert, I., Dale, A. M., & Einevoll, G. T. (2006). Current-source density estimation based on inversion of electrostatic forward solution: effects of finite extent of neuronal activity and conductivity discontinuities. *Journal of Neuroscience Methods*, **154**(1–2), 116–133.
- Pettersen, K. H., Lindén, H., Dale, A. M., & Einevoll, G. T. (2012). Extracellular spikes and CSD. *Handbook of Neural Activity Measurement*, **1**, 92–135.
- Rall, W. (1962). Electrophysiology of a dendritic neuron model. *Biophysical Journal*, **2**(2), 145–167.
- Scott, K. M., Du, J., Lester, H. A., & Masmanidis, S. C. (2012). Variability of acute extracellular action potential measurements with multisite silicon probes. *Journal of Neuroscience Methods*, **211**(1), 22–30.
- Somogyvári, Z., Cserpán, D., Ulbert, I., & Érdi, P. (2012). Localization of single-cell current sources based on extracellular potential patterns: The spike CSD method. *European Journal of Neuroscience*, **36**(10), 3299–3313.
- Somogyvári, Z., Zálányi, L., Ulbert, I., & Érdi, P. (2005). Model-based source localization of extracellular action potentials. *Journal of Neuroscience Methods*, **147**(2), 126–137.
- Steinmetz, N. A., Buettfering, C., Lecoq, J., Lee, C. R., Peters, A. J., Jacobs, E. A., Coen, P., Ollerenshaw, D. R., Valley, M. T., De Vries, S. E., Garrett, M., Zhuang, J., Groblewski, P. A., Manavi, S., Miles, J., White, C., Lee, E., Griffin, F., Larkin, J. D., ... Harris, K. D. (2017). Aberrant cortical activity in multiple GCaMP6-expressing transgenic mouse lines. *eNeuro*, **4**(5), ENEURO.0207–17.2017.
- Stuart, G., & Spruston, N. (1998). Determinants of voltage attenuation in neocortical pyramidal neuron dendrites. *Journal of Neuroscience*, **18**(10), 3501–3510.
- Tikhonov, A. N., & Arsenin, V. Y. (1977). *Solution of ill-posed problems*. Winston & Sons.
- Ting, J. T., Daigle, T. L., Chen, Q., & Feng, G. (2014). Acute brain slice methods for adult and aging animals: application of targeted patch clamp analysis and optogenetics. In *Patch-clamp methods and protocols* (pp. 221–242). Springer.
- Varona, P., Ibarz, M. J., López-Aguado, L., & Herreras, O. (2000). Macroscopic and subcellular factors shaping population spikes. *Journal of Neurophysiology*, **83**(4), 2192–2208.
- Wehr, M., Pezaris, J. S., & Sahani, M. (1999). Simultaneous paired intracellular and tetrode recordings for evaluating the performance of spike sorting algorithms. *Neuro-computing*, **26**, 1061–1068.
- Zhang, Y., Rózsa, M., Liang, Y., Bushey, D., Wei, Z., Zheng, J., Reep, D., Broussard, G. J., Tsang, A., Tsegaye, G., Narayan, S., Obara, C. J., Lim, J. X., Patel, R., Zhang, R., Ahrens, M. B., Turner, G. C., Wang, S. S. H., Korff, W. L., ... Looger, L. L. (2021). Fast and sensitive GCaMP calcium indicators for imaging neural populations. *bioRxiv*. <https://doi.org/10.1101/2021.11.08.467793>

Additional information

Data availability statement

The data that support the findings of the present study are available from the corresponding authors upon request. The scripts for implementing and analysing morphological and IC–EC voltage data are openly available online in our GitHub repository ([siCSDReconstruction-Project](https://github.com/siCSDReconstruction-Project)).

Competing interests

Zoltán Somogyvári is the owner and founder of Axoncord LLC. The other authors declare no competing interests.

Author contributions

Experiments were performed by the Integrative Neuroscience Group at the Institute of Cognitive Neuroscience and Psychology, Research Centre for Natural Sciences in Budapest, Hungary. D.M., Z.S., L.W. and I.U. conceived the experiments. D.M. performed the experiments. D.C., K.F. and Z.S. ran the simulations. A.B., P.B. and Z.S. implemented the software. D.M. and Z.S. analysed the results. D.M., A.B. and Z.S. wrote the manuscript. All authors approved the final version of the manuscript and agree to be accountable for all aspects of the work in ensuring that questions related to the accuracy or integrity of any part of the work are appropriately investigated and resolved. All persons designated as authors qualify for authorship, and all those who qualify for authorship are listed.

Funding

This research was supported by grants from the Hungarian National Research, Development and Innovation Fund (NKFIH K113147, K135837, K137886, PD143582 and RRF_2.3.1_21_2022_00015), the Human Brain Project associative grant CANON (under grant number NN118902), the Hungarian National Brain Research Program 2017-1.2.1-NKP-2017-00002 and 3.0, and the FLAG-ERA Joint Transnational Call 2021, VIPattract grant. The authors are grateful to the Eötvös Loránd Research Network for its support and the grant (SA-114/2021).

Acknowledgements

We thank László Négyessy, Gábor Nyíri, Kinga Tóth and Estilla Zsófia Tóth for their pieces of advice, providing infrastructure and technical help in the histological analysis and morphology reconstruction, Marcell Stippinger for his help in the video

processing, and Tamás Árpádfy-Lovas for his constructive criticism of the manuscript.

Keywords

brain slice, CA1, current source density, extracellular, ground truth, hippocampus, *in vitro*, intracellular, membrane potential, patch clamp, silicon probe, spike-triggered average

Supporting information

Additional supporting information can be found online in the Supporting Information section at the end of the HTML view of the article. Supporting information files available:

Statistical Summary Document
Peer Review History